



Geochemistry, Geophysics, Geosystems



RESEARCH ARTICLE

10.1029/2020GC009231

Key Points:

- Elastic thermobarometry has the potential to constrain pressures and temperatures of rocks from mantle, metamorphic, and magmatic settings
- Stiff inclusions that should preserve significant tension at ambient pressures may not be usable as elastic thermobarometers
- Feldspar inclusions are promising because of their high compressibility but are complicated by complex anisotropy

Supporting Information:

- Supporting Information S1
- Tables S1–S6
- · Data Set S1

Correspondence to:

M. Cisneros,

miguel.cisneros@erdw.ethz.ch

Citation:

Cisneros, M., & Befus, K. S. (2020). Applications and limitations of elastic thermobarometry: Insights from elastic modeling of inclusion-host pairs and example case studies. *Geochemistry, Geophysics, Geosystems, 21*, e2020GC009231. https://doi.org/10.1029/2020GC009231

Received 8 JUN 2020 Accepted 28 AUG 2020 Accepted article online 9 SEP 2020

Applications and Limitations of Elastic Thermobarometry: Insights From Elastic Modeling of Inclusion-Host Pairs and Example Case Studies

M. Cisneros^{1,2} and K. S. Befus³

¹Department of Geological Sciences, Jackson School of Geosciences, University of Texas at Austin, Austin, TX, USA, ²Now at Structural Geology and Tectonics Group, Geological Institute, Department of Earth Sciences, ETH Zürich, Zürich, Switzerland, ³Department of Geosciences, Baylor University, Waco, TX, USA

Abstract Elastic thermobarometry can be used to constrain the pressure and temperature conditions of mineral crystallization by exploiting the difference in the elastic evolution of a mineral inclusion and its host during cooling and decompression. In this work we examine the pressure-temperature sensitivity of >5,000 untested inclusion-host pairs. Hosts such as diamond and zircon are ideal host minerals because their low compressibility makes them rigid containment vessels. Highly compressible inclusions such as albite, graphite, and quartz serve as the most reliable barometers. We provide three case studies of inclusion-host pairs from different geologic settings to demonstrate the advantages and challenges associated with these mineral pairs. Apatite inclusions in olivine from Yellowstone caldera mostly record negative residual pressures (tension) and suggest magmatic crystallization at ~0.4 GPa. Rutile inclusions in garnet from Verpeneset eclogites record near ambient conditions and do not recover reasonable metamorphic conditions of rutile entrapment. These results suggest that stiff inclusions may have a tensile strain limit, a possible limitation of elastic thermobarometry. Albite inclusions in epidote from a blueschist (Syros, Greece) record geologically reasonable entrapment pressures, but a large range of residual pressures that may be caused by the complex anisotropy of both phases. Our theoretical and applied results indicate that elastic thermobarometry has the potential to be used to understand petrologic processes in diverse geologic environments, including mantle, metamorphic, and magmatic settings but that each elastic thermobarometer requires careful evaluation.

Plain Language Summary Determining the pressures and temperatures at which rocks forms is crucial to understanding processes that occur on Earth. The pressures and temperatures at which rocks form can give insights into processes such as the following: At what depths (pressures) do magmas form? How deep (pressure) do rocks go where continents or ocean plates collide? What are the conditions under which diamonds form? The geologic community has for many years developed methods to constrain the pressure and temperatures at which rocks form. Recent developments have tried to take advantage of the difference in the mechanical and physical properties of two minerals—one being trapped (inclusion) inside of another (host). The trapped mineral can retain some pressure at the Earth's surface, and we can try to estimate the initial conditions at which the inclusion was trapped by the host mineral. Here, we present new potential inclusion and host pairs that can be used to constrain these initial pressure and temperature conditions and discuss potential limitations associated with these mineral pairs. Some of these inclusion-host pairs may provide the potential to constrain the formation conditions of rocks that previously did not have suitable barometers or thermometers.

1. Introduction

Methods that can directly monitor geologic processes that occur in the deep subsurface do not exist. Active processes in magmatic, metamorphic, and mantle environments remain at the forefront of geoscience research because they control tectonism and crustal deformation, seismic and volcanic hazards, the geomorphic evolution of landscapes, and the generation of economic mineral resources. Much effort has been directed toward advancing methods to understand subsurface processes.

©2020. The Authors.

This is an open access article under the terms of the Creative Commons

Attribution License, which permits use, distribution and reproduction in any medium, provided the original work is properly cited.

CISNEROS AND BEFUS 1 of 21



Because we cannot visually observe these processes, we are forced to use indirect methods that include fieldwork and outcrop observations, petrography, geophysical methods, high pressure and temperature (P-T) experiments, and theoretical calculations. Accordingly, the P-T conditions of mineral and rock crystallization are central for understanding processes that influence crustal and mantle deformation, crystallization kinetics, molecular diffusion, and melt rheology. Many techniques, such as stable isotope thermometry, cation-exchange thermobarometry, graphite order-disorder thermometry, and thermodynamic modeling, have been developed to constrain P-T conditions of minerals (e.g., Beyssac et al., 2002; Ferry & Spear, 1978; Gualda et al., 2012; Javoy, 1977); however, these methods often have practical limitations imposed by the requisite mineralogy or equilibrium assumptions.

Elastic thermobarometry represents one increasingly important method used to determine P-T conditions of mineral crystallization (Adams et al., 1975a, 1975b; Angel et al., 2014; Cohen & Rosenfeld, 1979; Rosenfeld, 1969; Rosenfeld & Chase, 1961). Early researchers recognized that differences in the thermal expansivity and compressibility between a solid inclusion and host would generate quantifiable inclusion strain after eruption or exhumation (Adams et al., 1975a, 1975b; Cohen & Rosenfeld, 1979; Rosenfeld, 1969; Rosenfeld & Chase, 1961). Those strains are preserved by the inclusion and are related to the initial conditions when an inclusion was entrapped by a host mineral (e.g., Angel et al., 2014; Guiraud & Powell, 2006; Kohn, 2014). The calculations are solely dependent upon the physical properties of inclusion-host pairs. Thus, the technique has several key advantages in comparison to conventional thermobarometry based on chemical equilibrium. For example, neither chemical nor isotopic equilibrium among phases is required, and bulk-rock composition constraints do not exist. The technique also offers a high spatial resolution, commonly at the micron-scale, that allows constraining P-T conditions from inclusions within discrete subdomains of a single host crystal.

Recent work has improved the reliability and the applicability of elastic thermobarometry through some of the following advances: updated mineral thermodynamic properties (e.g., Angel, Alvaro, et al., 2017), by providing shape corrections for non-ideal inclusions (e.g., Mazzucchelli et al., 2018), by quantifying the effect of anisotropic strain on calculations (e.g., Murri et al., 2018; Stangarone et al., 2019; Zhong et al., 2019), by advancing the theory of the technique (e.g., Mazzucchelli et al., 2019; Zhong et al., 2018, 2020; Zhukov & Korsakov, 2015), by easing the implementation of elastic modeling for users (e.g., Angel, Mazzucchelli, et al., 2017), and by comparing entrapment conditions calculated from elastic thermobarometry with independent constraints or known experimental conditions of garnet synthesis (e.g., Bonazzi et al., 2019; Thomas & Spear, 2018). Elastic thermobarometry has primarily been applied to diamond- and garnet-hosted inclusions (e.g., Ashley et al., 2014; Cohen & Rosenfeld, 1979; Howell et al., 2010; Izraeli et al., 1999; Nestola et al., 2019; Thomas & Spear, 2018), because both of these host minerals are nearly isotropic and they should impose a near isotropic stress on the inclusions. However, recent work suggests that anisotropic inclusion-host pairs may similarly provide reliable P-T conditions (Cisneros et al., 2020), yet many inclusion-host pairs that could be used to extract P-T constraints have not been explored. Here, we evaluate the theoretical potential of >5,000 inclusion-host pairs as barometers or thermometers, building upon the work introduced by Kohn (2014) (48 inclusion-host pairs). Most of these inclusion-host pairs have never been tested, and significant additional work is needed to fully evaluate the inclusion-host pairs that we present. Our contribution solely presents the theoretical potential of a suite of diverse inclusion-host pairs.

We demonstrate three simple worked examples to illustrate advantages and challenges associated with these mineral pairs. Apatite inclusionsinolivine (ap-in-ol) from Yellowstone caldera and albite inclusions in epidote (ab-in-ep) from Syros, Greece, record a complex array of entrapment conditions; however, some calculated entrapment pressures agree with P-T constraints from previous studies. Residual inclusion pressures recorded by rutile inclusions in garnet (ru-in-grt) in an eclogite from Verpeneset, Norway, are far different than expected residual pressures based on established metamorphic conditions of garnet growth and may suggest that stiff inclusions in hosts have a tensile strain limit. We also provide a script with a graphical user interface (GUI) that allows for evaluation of our code. The script can be used to calculate entrapment pressures and temperatures and allows linear mixing of molar volumes and shear moduli to account for mineral solid solutions.

CISNEROS AND BEFUS 2 of 21



2. Methods

2.1. Elastic Modeling Calculations: An Overview

The difference in compressibility and thermal expansivity between a crystalline inclusion and host generates compression or expansion of the inclusion as P-T conditions change. At ambient temperatures, encapsulated inclusions preserve a residual strain, which can be converted to an inclusion pressure (P_{inc}). Residual strains can be quantified by multiple techniques, including measurement of birefringent halos surrounding inclusions (e.g., Howell et al., 2010; Rosenfeld & Chase, 1961), X-ray Diffraction (e.g., Harris & Munn, 1970; Nestola et al., 2011), and by the approach we implement in this study, Raman Spectroscopy (e.g., Ashley et al., 2014; Enami et al., 2007). The residual inclusion pressure can be combined with elastic modeling to calculate the initial entrapment pressure (P_{trap}) or temperature (T_{trap}) (e.g., Adams et al., 1975a, 1975b; Rosenfeld, 1969; Rosenfeld & Chase, 1961; Van der Molen & Van Roermund, 1986; Zhang, 1998).

To calculate entrapment pressures and temperatures, we perform one-dimensional elastic modeling to determine the elastic response of inclusion-host pairs upon return to ambient conditions. We implement the elastic model derived by Angel, Mazzucchelli, et al. (2017, equation A5):

$$\left[\left(\frac{V}{V_{\text{trap}}} \right)_{inc} - \left(\frac{V}{V_{\text{trap}}} \right)_{host} \right] \left(\frac{V_{\text{trap}}}{V_{foot}} \right)_{inc} = \frac{3}{4G_{host}} (P_{inc} - P_{ext}), \tag{1}$$

where $(V/V_{trap})_{inc}$ and $(V/V_{trap})_{host}$ are the molar volume ratios of the entrapped inclusion and the free host at measurement (V) and entrapment (V_{trap}) conditions, respectively. $(V_{trap}/V_{foot})_{inc}$ is the ratio of the inclusion molar volume at entrapment conditions and at ambient temperature along the inclusion-host pair isomeke (V_{foot}) (e.g., Angel, Mazzucchelli, et al., 2017). G_{host} , and P_{ext} are the shear modulus of the host and ambient pressure (0.1 MPa), respectively. P_{inc} is the residual pressure of the inclusion at measurement conditions. To calculate entrapment conditions with Equation 1, a unique solution is identified by iteratively calculating V_{trap} until both sides of the equation are equal (e.g., Ashley et al., 2016; Angel, Mazzucchelli, et al., 2017; Guiraud & Powell, 2006; Kohn, 2014). V_{trap} is a function of both the pressure and temperature of entrapment. Therefore, for many inclusions-host pairs it is necessary to constrain the temperature or pressure of entrapment so that the second unknown variable can be accurately determined. Equation 1 can also be solved to determine how the residual P_{inc} changes across P-T space. The points in P-T space that represent solutions to a constant P_{inc} have been referred to as isomekes ("iso" = equal, meke = "length") (Adams et al., 1975a, 1975b). Isomeke lines represent points in P-T space along which fractional volume (V) changes of an inclusion and host are equal:

$$\frac{\partial V_{host}}{V_{host}} = \frac{\partial V_{inc}}{V_{inc}}.$$
 (2)

The instantaneous slope of an isomeke line can be defined by the equation

$$\left(\frac{\partial P}{\partial T}\right)_{(V_{inc} - V_{host})} = \frac{\alpha_{inc} - \alpha_{host}}{\beta_{inc} - \beta_{host}},\tag{3}$$

where V, α , and β , are the molar volume, thermal expansivity, and compressibility of the inclusion and host, respectively (Angel et al., 2015) (Table 1). The instantaneous slope is useful for evaluating if inclusion-host pairs are suitable barometers or thermometers and can also be used to constrain the curvature of isomekes. Isomekes often occur as nearly straight lines at geologically relevant conditions but sometimes exhibit curvature due to nonlinear responses of some minerals to changing P-T conditions (e.g., minerals that undergo phase transitions); isomekes should be carefully evaluated when working with minerals that potentially undergo phase transitions (e.g., titanite, quartz, calcite, and ilmenite). For example, quartz-in-host isomekes become increasingly nonlinear as temperatures approach the quartz α - β transition. Furthermore, at absolute zero (T = 0 K) thermal expansivities are zero, and thus, the isomeke slope is zero ($\frac{\partial P}{\partial T}|_{isomeke} = 0$), but the slope is nonzero above this temperature (Angel et al., 2015; Rosenfeld & Chase, 1961).

CISNEROS AND BEFUS 3 of 21



Table 1 Abbreviations Often Used Throughout To	This Manuscript
Abbreviation	Definition
α	Thermal expansivity of inclusion or host
eta K	Compressibility of inclusion or host Bulk modulus of inclusion or host $(K = \beta^{-1})$
$(\partial P/\partial T)_{isomeke}$ dP/dT	Instantaneous slope of an isomeke ^a Estimated slope of an isomeke ^b
θ	Angle of isomeke slope (dP/dT) relative to the x axis
$κ$ ω_{inc}	Estimated curvature of an isomeke Wave number position of an inclusion
ω_{ref}	Wave number position of a reference or standard
$\Delta\omega$ P_{inc}	$\Delta\omega = \omega_{inc} - \omega_{ref}$ Inclusion pressure calculated from hydrostatic calibrations that determine the pressure-dependence of $\Delta\omega$
P_{trap}	Entrapment pressure
T_{trap} s.d.	Entrapment temperature Standard deviation

^aSee text for discussion on isomekes. ^bSlope of isomeke that is approximated as being linear.

Isomeke slope and spacing are important criteria for elastic thermobarometry (e.g., Angel et al., 2015; Kohn, 2014). Inclusion-host pairs with steep isomeke slopes make the best thermometers (high $[\partial P/\partial T]_{isomeke}$; e.g., zircon inclusions in garnet), whereas those with shallow slopes (low $[\partial P/\partial T]_{isomeke}$; e.g., quartz inclusions in garnet) are the best barometers. Intermediate isomeke slopes allow either P_{trap} or T_{trap} to be determined but require a good independent constraint of one of the variables. Isomeke spacing indicates the sensitivity of a thermobarometer to a change in a residual inclusion pressure, that is, the amount that P_{trap} or T_{trap} changes with a change in P_{inc} . To calculate the slope and the spacing between isomekes, we assume that isomeke lines are linear. To quantify if a linear approximation is appropriate at geologically relevant conditions, we estimate the curvature (κ) of isomekes by calculating the difference in the angle (Θ) of an isomeke slope (dP/dT, relative to the x axis) across two T_{trap} windows ($T_{trap} = 500-700^{\circ}$ C; $700-900^{\circ}$ C). All isomeke curvature, slope, and spacing results are provided in the supporting information (Tables S1 and S2).

2.2. Molar Volume Calculations and Thermodynamic Properties

To perform molar volume calculations, we used thermodynamic properties from various sources (sources provided in the supporting information). Most of the thermodynamic properties were derived from the Holland and Powell (2011) database. We use the modified Tait Equation of State (EoS) and thermal pressure term to solve for molar volumes at given P-T conditions (Holland & Powell, 2011). We implement Landau and Braggs-William theory to calculate excess molar volumes that are associated with spontaneous strain development of phases that undergo phase transitions (e.g., Holland & Powell, 1996a, 1996b, 1998, 2011). To model quartz volumes, we use the thermodynamic properties and the curved-boundary modeling approach from Angel, Alvoro, et al. (2017). Because we use apatite, epidote, garnet, and rutile in our case studies, we use updated thermodynamic properties to model the molar volumes of these phases. To model apatite and epidote molar volumes, we use the thermodynamic properties given in Ashley et al. (2017) and Cisneros et al. (2020), respectively, which are derived from previous P-V-T experiments (apatite: Brunet et al., 1999; Hovis et al., 2014, 2015; Schouwink et al., 2010; epidote: Gatta et al., 2011; Pawley et al., 1996; Qin et al., 2016) and the Tait EoS with a thermal pressure term. To model grossular garnet, we use the P-V-T experiments and thermodynamic properties of Milani et al. (2017) and a Tait EoS with a thermal pressure term. To calculate rutile molar volumes, we use the revised thermodynamic properties and modeling approach of Zaffiro et al. (2019), which implements a Birch-Murnaghan third-order EoS and a Kroll thermal model. We account for solid solutions of apatite (OH-Cl-F) inclusions and garnet, olivine (Fe-Mg), and epidote-clinozosoite (Al-Fe) hosts by implementing ideal (linear) mixing of end-member molar volumes. This approximation has been shown to be appropriate for apatite (Hovis et al., 2015), olivine (Speziale et al., 2004), and epidote (Cisneros et al., 2020; Franz & Liebscher, 2004). Variations in molar volume between almandine-pyrope garnet solid solutions exhibit ideal behavior (Milani et al., 2015). Variations in molar volume between almandine-grossular garnet solid solutions exhibit slight nonideal behavior

CISNEROS AND BEFUS 4 of 21



(Cressey et al., 1978), and pyrope-grossular solid solutions exhibit greater nonideal behavior (Geiger, 2000); thus, our linear approximation may introduce additional errors in our final P_{trap} calculations. However, the difference in molar volume between pure almandine and grossular end-members far exceeds the difference between ideal and nonideal molar volume estimations, and not accounting for mixing introduces greater uncertainties. A comparison of P_{trap} calculated from EoSFit-Pinc (Angel, Mazzucchelli, et al., 2017) and our script is provided in the supporting information (Table S3); this accounts for reproducibility of molar volume and elastic modeling calculations.

For minerals that have experimentally determined shear moduli, we use those shear moduli in our calculations. Otherwise, the shear modulus of the host is calculated from mineral Poisson ratios and bulk moduli, following the equation

$$G_{host} = \frac{3K_{host}(1 - 2\nu_{host})}{2(1 + \nu_{host})}; K_{host} = \frac{1}{\beta_{host}},$$
 (4)

where G_{host} , K_{host} , and ν_{host} are the shear modulus, bulk modulus, and Poisson ratio of the host phase. Shear moduli and Poisson ratios were compiled from the literature and are provided in the supporting information. We provide further reference information on the host shear moduli that we use in our case studies. For fayalite and forsterite, we use the experimentally determined shear moduli from Speziale et al. (2004) ($G_{fa}=51.2~{\rm GPa}$; $X_{fa}=0.94$) and Zha et al. (1996) ($G_{fo}=82.0~{\rm GPa}$; $X_{fo}=1$), respectively. For garnets, we use the shear moduli of Wang and Ji (2001) ($G_{alm}=92.1~{\rm GPa}$, $G_{prp}=90.2~{\rm GPa}$, $G_{sps}=96.3~{\rm GPa}$); however, for grossular garnet we use the shear modulus of Isaak et al. (1992) ($G_{grs}=106.9~{\rm GPa}$). A shear modulus has been experimentally determined for epidote ($G_{ep}=61.2~{\rm GPa}$, Ryzhova et al., 1966); however, we are not aware of experimental shear modulus data for clinozoisite. To maintain consistency, we calculate the shear moduli of epidote group minerals by using Equation 7, with the aggregate Poisson's ratio of 0.26, from Mao et al. (2007) and the regressed bulk moduli from Cisneros et al. (2020) ($G_{ep}=65.7~{\rm GPa}$, $G_{cz}=84.0~{\rm GPa}$, and $G_{zo}=59.7~{\rm GPa}$). We implement ideal mixing of shear moduli to account for solid solutions of host phases. We limit our inclusion-host pair calculations to 72 phases with reported shear moduli or Poisson ratios (Table S1).

2.3. Analytical Techniques

For each case study, we petrographically identified hosts containing mineral inclusions. We identified apatite inclusions in olivine and rutile inclusions in garnet in grain mounts of handpicked crystals. Albite inclusions in epidote were identified in $\sim 80 \, \mu m$ -thick petrographic sections. Inclusions were isolated and two-to-three times the inclusion radial distance from the host exterior, fractures, cleavage, or other inclusions (e.g., Campomenosi et al., 2018; Mazzucchelli et al., 2018; Zhang, 1998; Zhong et al., 2020).

We performed analyses with Raman systems at Baylor University and Virginia Tech. Measurements at Baylor University (ap-in-ol and ru-in-grt) were carried out on a Thermoscientific DXR Raman microscope with 1,600 lines mm⁻¹ grating. Measurements used a 532 nm laser with 10 mW laser power at the sample surface and a 100X objective, which allowed a spatial resolution of 1 μm. The 1,000 cm⁻¹ band of polystyrene was used for standardization. Measurements at Virginia Tech (ab-in-ep) were carried out on a JY Horiba LabRam HR800 Raman Spectrometer with 1,800 lines mm⁻¹ grating, and a 100X objective with a 0.9 numerical aperture. A 514 nm Ar laser was used for analyses, and the 520.3 cm⁻¹ plasmaline was used to simultaneously correct feldspar measurements for drift by applying a linear drift correction (Table 2; Figure 3). Based on the long-term repeat measurements of the ~291, 479, and 507 cm⁻¹ bands of Amelia Albite, peak position uncertainty at Virginia Tech is $\pm 0.1~{\rm cm}^{-1}$. No thermal corrections were applied to the measured Raman spectra. A linear background subtraction was simultaneously applied to the spectra during peak fitting of inclusion and host Raman bands, and the Ar plasmaline (only VT analyses). We used a Voigt Area model within PeakFit v4.12 (by Systat Software Inc) to fit the ~964 cm⁻¹, and ~291 cm⁻¹, ~479 cm⁻¹ and ~507 cm⁻¹ bands of apatite, and albite, respectively, and a Pearson IV model to fit the ~444 cm⁻¹ and 609 cm⁻¹ bands of rutile; a Gaussian area model was used to fit the 520.3 cm⁻¹ Ar plasmaline (Figure 3). Quartz inclusions in garnet (qtz-in-grt) were also measured by Raman spectroscopy to compare with results from the ab-in-ep barometer. Further information about peak fitting inclusion and host bands and details about qtz-in-grt measurements and calculations are provided in the supporting information (Tables S5

CISNEROS AND BEFUS 5 of 21

Table 2 Raman M	Table 2 Raman Measurements of Inclusions From Each of the Three	f Inclusion:	s From Each	of the Thre	e Case Studies	lies										
Apatite											Rutile					Albite
Analysis ^a	$\omega (\mathrm{cm}^{-1})$	$\Delta \omega^{\mathrm{b}}$ (cm^{-1})	P_{inc} (MPa)	Error (MPa)	P_{trap} (GPa)	Error (GPa)	Analysis ^a	$\omega (\mathrm{cm}^{-1})$	$\Delta \omega \ (\mathrm{cm}^{-1})$	P_{inc} (MPa)	Error (MPa)	$\omega (\mathrm{cm}^{-1})$	$\Delta \omega \ (\mathrm{cm}^{-1})$	P_{inc} (MPa)	Error (MPa)	Analysis ^c
1	962.6	0.3	61	97	1.70	0.67	1	443.7	0.4	19	62	609.2	0.0	-2	93	1
2	961.3	-1.0	-228	96	-0.04	0.53	2	443.5	0.2	-10	61	609.5	0.3	26	93	2‡
3	961.8	-0.5	-117	6	0.58	0.59	3	444.6	1.3	159	99	609.2	0.0	-2	93	3÷
4	961.8	-0.5	-107	96	0.64	0.59	4	443.8	0.5	38	62	609.1	-0.1	-25	93	+ 4
5	961.3	-1.0	-235	96	-0.08	0.53	5	444.3	1.0	105	65	6.609	0.7	159	95	5
9	961.7	9.0-	-145	26	0.42	0.57	9	444.6	1.3	163	29	609.1	-0.1	-18	93	
7	961.3	-1.1	-241	96	-0.11	0.53	7	443.8	0.5	35	62	609.5	0.2	55	93	7
~	961.6	-0.7	-161	96	0.33	0.56	∞	444.7	1.4	168	29	609.4	0.2	47	94	8
6	962.2	-0.2	-38	26	1.06	0.62	6	444.9	1.6	206	89	2.609	0.5	109	94	116
10	961.4	6.0-	-203	96	0.10	0.54	10	445.3	2.0	265	72	610.3	1.1	232	95	Average
Average	961.7 (0.4)c	0.6	-141 (96)		0.5 (0.6)		11	443.4	0.1	-18	61	609.3	0.1	19	93	
							12	444.2	6.0	92	4	9.609	0.4	77	94	
							Average	444.2 (0.6)	(9.0) 6.0	135 (92)		609.5 (0.3)	0.3 (0.3)	59 (77)		
Note. n.d.	Note. n.d. = not detected. ^a Analyses carried-out at Bavlor. ^b Peak positions (ω) of unstrained references are $\omega_{nnnito} = 962.3$ cm ⁻¹ ; $\omega_{nnito} =$	ted. ^a Ana	lvses carried	-out at B	avlor. ^b Pea	k positior	ın Jo (ω) sı	nstrained ref	ferences ar	e Wanatite	= 962.3	cm^{-1} : $\omega_{m,ril}$	$_{o} = 443.3 \text{ cm}^{-1}$		d 609.2 c	and 609.2 cm^{-1} ; and

 $\sim_{anone} - \sim_{coco}$ and \sim_{coco} are \sim_{coco} and \sim_{coco} are \sim_{coco} and \sim_{coco} are \sim_{coco} and \sim_{coco} and \sim_{coco} are \sim_{coco} and \sim_{coco

and S6). Raman uncertainties that are reported propagate errors of simultaneous background subtraction and peak fit statistics of inclusion-host Raman bands, Ar plasmaline fit statistics (only Virginia Tech analyses), and instrument uncertainty (± 0.1 cm⁻¹ at VT and ± 0.3 cm⁻¹ at Baylor). P_{inc} errors propagate Raman uncertainties and errors of constants from polynomial fits to data from hydrostatic experiments (Figure S4; Table S4).

Fully encapsulated inclusions preserve strain that causes the Raman active vibrational modes of inclusions to be shifted to higher or lower wave numbers relative to minerals that are unstrained (fully exposed). We calculate the Raman shift(s) of inclusions (ω_{inc}) relative to Raman shift(s) of individual separated grains (apatite and rutile, ω_{ref}), and an unencapsulated standard (amelia albite; ω_{ref}) at ambient conditions ($\Delta \omega = \omega_{inc} - \omega_{ref}$). To calculate residual inclusion pressures (P_{inc}) of minerals, we use pressure-dependent Raman shift(s) $(P-\Delta\omega)$ relationships that have been calibrated under hydrostatic stress conditions by using hydrothermal diamond anvil cell experiments (HDAC), for example, apatite (Comodi et al., 2001; Schouwink et al., 2010); feldspar: (Aliatis et al., 2017; Befus et al., 2018); anatase/rutile: (Liu & Mernagh, 1992; Samara & Peercy, 1973; Swamy et al., 2005); and quartz/coesite: (Asell & Nicol, 1968; Hemley, 2013; Schmidt & Ziemann, 2000). The pressure-dependent Raman shift(s) of vibrational modes of many other minerals remain unconstrained. Recent work has explored the effects of nonhydrostatic stress on Raman active vibrational modes of minerals by using density functional theory strain- $\Delta\omega$ simulations to determine Grüneisen tensors that can be used to convert mineral Raman shifts ($\Delta\omega$) to strains (e.g., Murri et al., 2018; Nestola et al., 2018; Stangarone et al., 2019). However, we use hydrostatic P- $\Delta \omega$ calibrations to calculate residual P_{inc} because no Grüneisen tensors have been determined for apatite, rutile, and feldspar. Some work suggests that apatite inclusions in garnet develop minimal anisotropy when heated at ambient pressure (Ashley et al., 2017); therefore, not accounting for anisotropic strain of apatite inclusions may introduce minimal errors. This estimation may be erroneous for rutile and albite inclusions.

3. Results

3.1. Inclusion-Host Pair Modeling

We test the pressure-temperature sensitivity of 5,142 inclusion-host pairs by carrying out entrapment P-T calculations to produce isomekes in P-T space (Figure 1). We calculated the slope and spacing of the resulting isomekes by assuming they are linear and parallel. We acknowledge that our assumption may misrepresent isomekes that are nonlinear (e.g., calcite or quartz inclusions produce curved isomekes). However, the majority of inclusion-host pairs produce near linear isomekes with curvature (κ) less than 2° at geologically relevant conditions (500–900°C); a curvature \leq 2° is equal to a change in slope of \leq 0.035 MPa °C⁻¹. Of the >5,000 pairs we analyzed, 75% have isomekes that curve less than 2°, and 86% curve less than 5° across the 400°C window (Table S2). Treatment of these isomekes as linear functions is an appropriate approximation, albeit,

CISNEROS AND BEFUS 6 of 21

Continued

	Error (GPa)	0.20	23	20	33	0.23	48	1.05	1.91	0.62			and rec-
		0.	0.	0.	0.	0.	0.	1.	1.	0.	(s)		cm^{-1} ; lrift cor a weigh an P_{in} lyzed n
	P _{trap} (GPa)	1.39	1.13	1.53	1.19	1.01	1.39	1.96	1.10	1.93	1.4(0.3)	1.3 (0.2)	and 609.2 cm ⁻¹ ; and ng a linear drift correc- We assign a weight to analyses mean P_{inc} .
	Error ^e (MPa)	89	81	99	113	81	96	262	341	192		7	cm ⁻¹ and applying a sis 5). We each anal tion (σ) of
	Mean P_{inc}^{e} (MPa)	505	416	552	437	371	503	691	402	682	506(116)	483(76) ^g	ite = 443.3 corrected by from Analy relative to ndard devia
	Error (MPa)	101	118	142	109	158	86	133	115	121		7	n^{-1} ; ω_{rut} ; ositions c two bands each band ant the sta
	P_{incl} (MPa)	480	909	533	641	551	614	765	327	728	583 (132)		= 962.3 cr th. dPeak pan than bands (ated from eated from eaters
	$\Delta \omega$ (cm-1)	6.0	1.2	1.1	1.3	1.1	1.2	1.5	0.7	1.4	1.1(0.2)		e ωapatite Irginia Tec albite Ram Pinc calculà in parenth
ite	ω^{d} (cm-1)	508.4	508.7	508.5	508.7	508.6	508.7	508.7	507.9	508.6	508.5 (0.3)		Hor. Peak positions (ω) of unstrained references are $\omega_{apadite} = 962.3$ cm ⁻¹ ; $\omega_{nuile} = 443.3$ cm ⁻¹ and 609.2 cm ⁻¹ ; and 507.5‡ and 507.2 \parallel cm ⁻¹ . Analyses carried-out at Virginia Tech. ⁴ Peak positions corrected by applying a linear drift corrected by weighting (ω) the P_{inc} error from all three albite Raman bands (two bands from Analysis 5). We assign a weight to error is calcuated from the weighted variance of P_{inc} calculated from each band relative to each analyses mean P_{inc} . ⁸ Weighted mean P_{inc} of all analyses. ^h Values in parentheses represent the standard deviation (σ) of the analyzed meaveighted mean P_{inc} of all analyses.
Albite	Error (MPa)	53	49	118	52	71	77	100	81	91			strained 1 talyses car to error fr veighted 1 veighted 2 all analyse es.
	P_{inc} (MPa)	473	380	456	375	334	420	383	104	457	376 (112)		(ω_{-1}) of unce (ω_{-1}) of unce (ω_{-1}) can (ω_{-1}) from the vertice (ω_{-1}) and (ω_{-1}) of all analys
	$\begin{array}{c} \Delta\omega \\ (\mathrm{cm}^{-1}) \end{array}$	1.8	1.4	1.7	1.4	1.2	1.6	1.4	0.4	1.7	1.4(0.4)		c positions and 507.2 y weighting calcuated eighted me nean Pinc C
	$\omega^{ m d}$ (cm-1)	481.0	480.7	480.9	480.6	480.5	480.8	480.5	479.5	480.8	480.6 (0.5)	4	Baylor. $^{\mathrm{D}}$ Peak $^{\mathrm{n}}$, 507.5† a calculated by $^{\mathrm{p}}$ inc error is an $^{\mathrm{E}}$ inc. $^{\mathrm{g}}$ We weighted m
	Error (MPa)	102	250	85	232	I	203	104	26	93			-out at $ +$ 79.1 $ $ cr $ +$ 79.1 $ $ cr $ +$ 6 mean ghted me from th
	P_{inc} (MPa)	655	521	809	653		612	973	887	889	725 (166)		yses carried 479.2‡ and line ω . ${}^{\circ}M$ = $1/\sigma_i^2$. The om the weigon the calculated
	$\begin{array}{c} \Delta \omega \\ (\mathrm{cm}^{-1}) \end{array}$	1.4	1.1	1.3	1.4	1	1.3	2.1	2.0	2.0	1.6 (0.4)		ted. ^a Anal $0.5 \parallel \text{cm}^{-1}$, Ar plasma of of $w_i = 1$ Iculated from the collision of $w_i = 1$
	Analysis ^a $\omega^{\rm d} ({\rm cm}^{-1}) ({\rm cm}^{-1})$	292.2	291.9	292.1	292.2	n.d.	292.1	292.7	292.5	292.5	292.3 (0.2) 1.6 (0.4) 725 (166)		Note. n.d. = not detected. ^a Analyses carried-out at Baylor. ^b Peak positions (ω) of unstrained references are $\omega_{apaite} = 962.3$ cm ⁻¹ ; $\omega_{rutile} = 443.3$ cm ⁻¹ and 609.2 cm ⁻¹ ; and $\omega_{abbite} = 290.8$; and 290.5ll cm ⁻¹ , 479.2; and 479.1ll cm ⁻¹ , 507.5f and 507.2ll cm ⁻¹ . ^c Analyses carried-out at Virginia Tech. ^d Peak positions corrected by applying a linear drift correction based on the 520.3 Ar plasmaline ω , ^e Mean P_{inc} calculated by weighting (ω) the P_{inc} error from all three albite Raman bands (two bands from Analysis 5). We assign a weight to the P_{inc} from each band of $\omega_i = 1/\sigma_i^2$. The mean P_{inc} error is calculated from the weighted variance of P_{inc} calculated from the weighted mean P_{inc} . ^b Weighted mean P_{inc} of all analyses. ^h Values in parentheses represent the standard deviation (σ) of the analyzed measurements and calculations. ¹ P_{tran} calculated from the weighted mean P_{inc} of all analyses.
Apatite	Analysis ^a	1	2	3	4	5	9	7	8	6	10	Average	Note. n.d. $\omega_{albite} = 2!$ tion based the P_{inc} fr $^{f}T_{trap} = 45$ surements

minimal errors are introduced (calculations and results provided in Tables S1 and S2). The subsequent results we present serve as a first-order guide, but users should carefully examine the specific isomeke slope and spacing of a target inclusion-host pair.

Isomekes were constructed by solving for P_{trap} in Equation 1, using $P_{inc} = -200$ to 800 MPa and $T_{trap} = 300^{\circ}\text{C}$ to 1,000°C, with 100 MPa and 100°C intervals, respectively. Isomeke slopes vary from 0.04 to $10^{5.1}$ MPa °C⁻¹, with a median value of 1.8 MPa °C⁻¹ (Figures 1a, 1c, and 1e; Table S1). Pairs at the 16th and 84th percentiles have isomekes slopes that are \leq 0.5 and 5.6 MPa °C⁻¹, respectively (Figure 1a). At the median, an isomeke slope of 1.8 MPa °C⁻¹ indicates that if the T_{trap} estimate changes by 100°C, the calculated final P_{trap} changes by 0.18 GPa (e.g., quartz-in-almandine; Figure 1a).

We measured isomeke spacing perpendicular to isomeke lines (Equation S2); hence, the units may be considered to be between MPa (horizontal isomekes) and °C (vertical isomekes); we do not give an exact spacing unit. Isomeke spacing was calculated by measuring the distance between the 100 and 200 MPa isomekes at $T_{trap} = 500$ °C. Isomeke spacing ranges from ~0 up to $10^{4.3}$, with a median of 193. The 16th and 84th percentiles of inclusion-host pairs having isomeke spacings that are ≤92 and 383, respectively (Figure 1d). Isomeke spacing of a single inclusion-host pair can vary between different isomekes and in P-T space, but we use our spacing calculation as a representative estimate that allows us to compare spacing with other inclusion-host pairs. We refer to sensitivity in terms of isomeke spacing. The relative terms "high sensitivity" and "low sensitivity" refer to smaller and greater isomeke spacing, respectively. Small isomeke spacing (high sensitivity) indicates that a large change in P_{inc} causes a small change in P_{trap} or T_{trap} (Figure 1b). Tightly spaced isomekes reduce uncertainty in the final P_{trap} or T_{trap} , because the error associated with the residual P_{inc} produces a smaller change in P_{trap} or T_{trap} . We note that our description of sensitivity does not refer to the sensitivity of $\Delta\omega$ to $P(P-\Delta\omega)$ relationships from hydrostatic calibrations) and is independent of this relationship.

3.2. Case Studies

We present introductory case studies for three inclusion-host pairs from different geologic environments and discuss the Raman bands that correspond to specific vibrational modes (ν_x) that we focused on analyzing to calculate residual P_{inc} . We present few analyses for the studied inclusion-host pairs, and we emphasize that these calculations only serve as illustrations and do not quantify the applicability of the studied pairs.

3.2.1. Apatite-in-Olivine: An Igneous Rock Application

Volcanologists and igneous petrologists use the P-T conditions of magmatic rocks to better understand melt genesis, assimilation and fractional crystallization, eruption triggers, and melt transport. Magma composition controls the mineral phases that may crystallize, and the diversity of magma compositions permits many potential inclusion-host pairs to be considered as elastic thermobarometers.

CISNEROS AND BEFUS 7 of 21

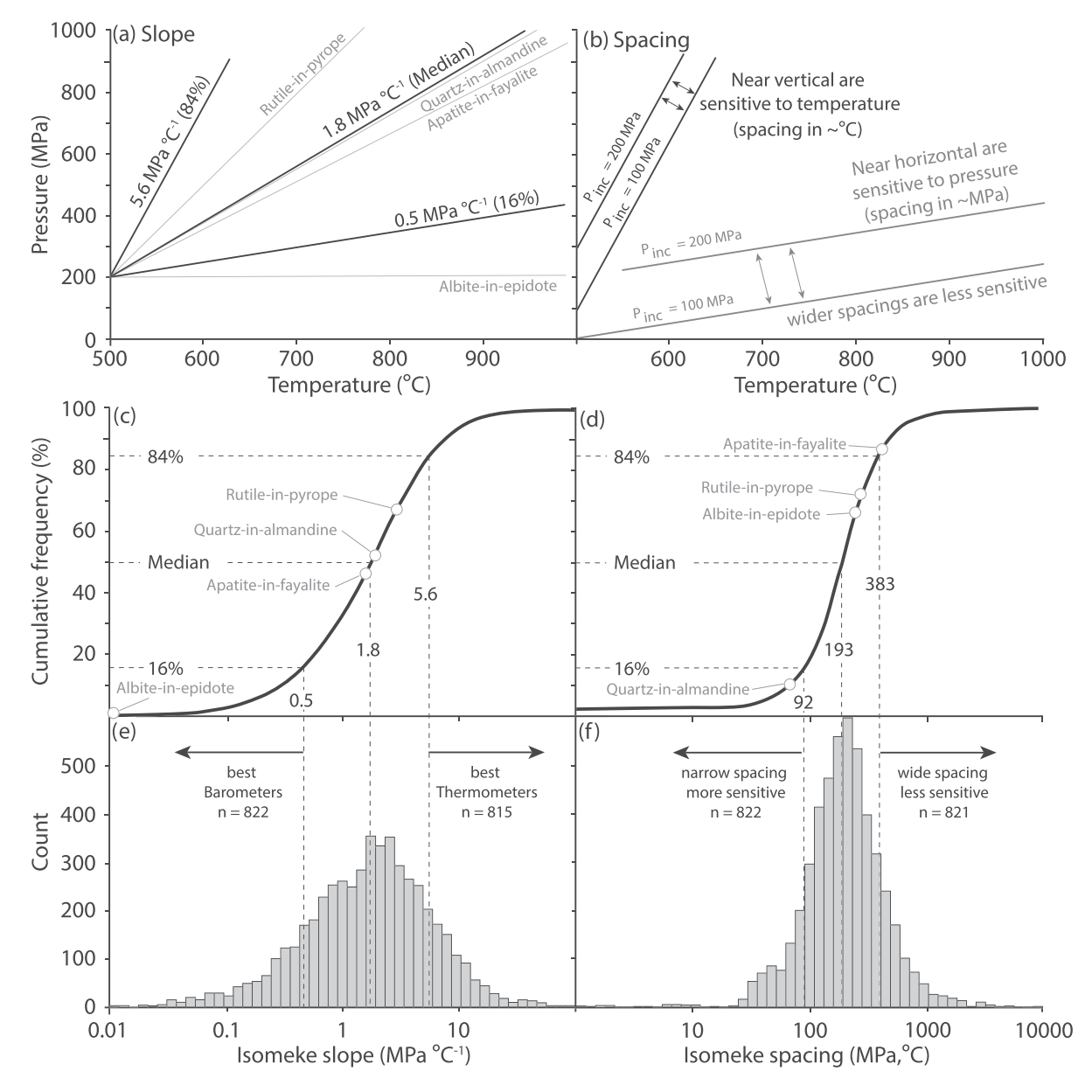


Figure 1. (a) Isomeke slopes for inclusion-host pairs. Representative inclusion-host pairs are chosen to illustrate excellent barometers (slope ≤0.5 MPa $^{\circ}$ C⁻¹) and thermometers (slope ≥5.6 MPa $^{\circ}$ C⁻¹). Pairs that fall in between these end-members require independent constraints to calculate the unknown variable of interest. (b) Spacing between isomekes is a metric of sensitivity. Wide spacing between isomekes indicates that a small change in P_{inc} will produce large changes in P_{trap} or T_{trap} . Small spacing between isomekes indicates that a small change in P_{inc} will produce small changes in P_{trap} or T_{trap} . We note that spacing calculations are unit-dependent, calculations using GPa units would results in different absolute values, but we are only concerned with relative differences. (c-f) Cumulative frequency and histogram plots indicating the proportion of inclusion-host pairs that serve as barometers or thermometers and their sensitivities. Most inclusion-host pairs serve as thermobarometers that require independent entrapment pressure or temperature estimates to derive the unknown variable (entrapment P or T).

We first examine apatite inclusions hosted by olivine phenocrysts (ap-in-ol) from the rhyolitic obsidian Solfatara Plateau Lava flow in Yellowstone caldera (Figures 2a, 2d, and 2g). Apatite is rarely used as an inclusion, but previous studies have shown that apatite inclusions in garnet can record reasonable conditions of garnet growth in skarn deposits (Barkoff et al., 2017, 2019). Elastic modeling shows that for ap-in-ol, over the window of $T_{trap} = 500^{\circ}\text{C}$ to 900°C and $P_{inc} = 200$ MPa: $\kappa = 0.7^{\circ}$, $dP/dT \approx 1.7$ MPa °C⁻¹ (Figures 1a and 1c), and between the -200 and -100 MPa P_{inc} isomekes at $T_{trap} = 500^{\circ}\text{C}$, spacing ≈ 280 (Figure 1d). The isomeke

CISNEROS AND BEFUS 8 of 21

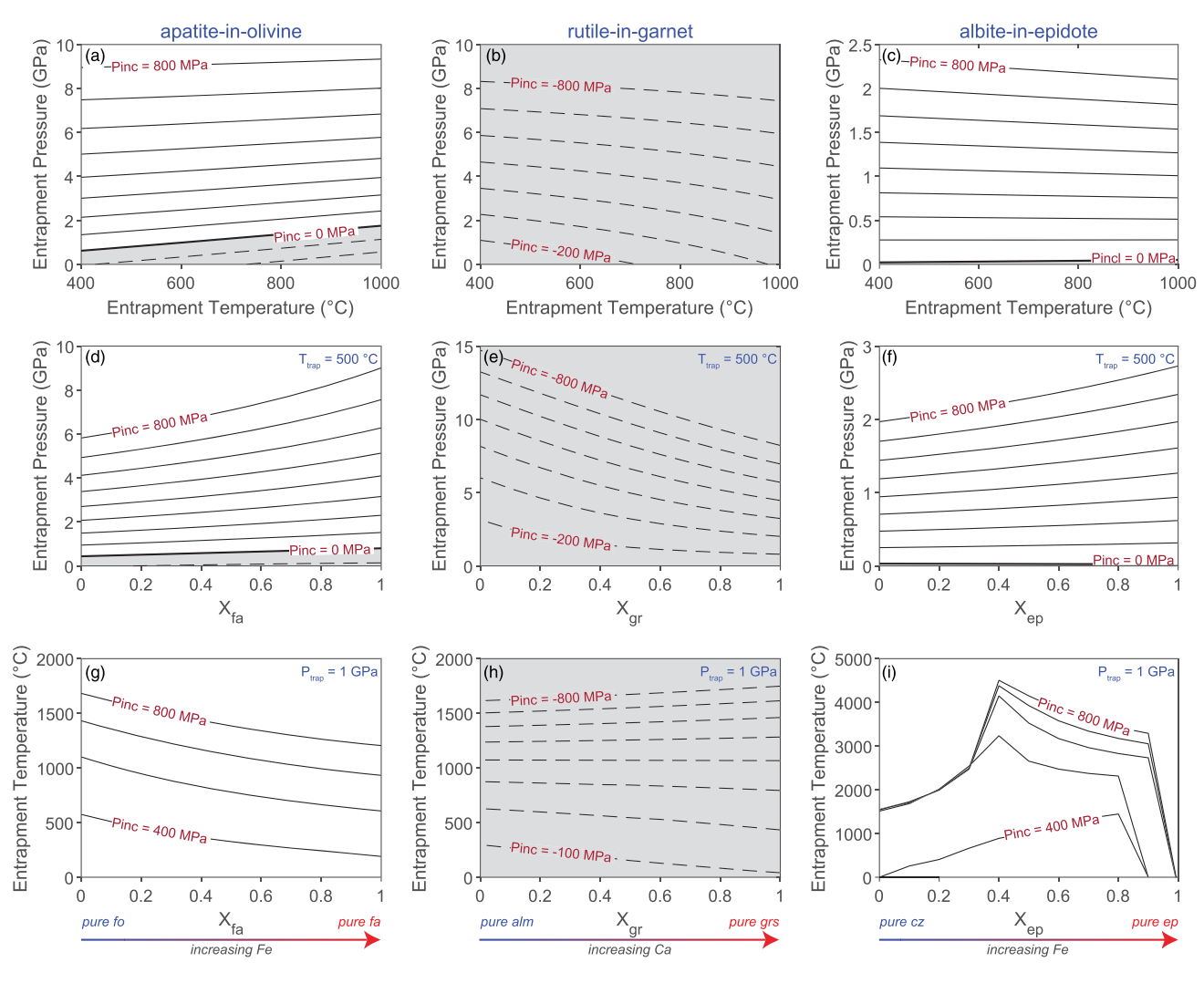


Figure 2. Isomekes graphs for (a, d, and g) apatite-in-olivine ($X_{ap-fluoro} = 1$, $X_{fa} = 1$), (b, e, and h) rutile-in-garnet ($X_{ru} = 1$, $X_{gr} = 1$), and (c, f, and i) albite-in-epidote ($X_{ab} = 1$, $X_{ep,cz} = 0.5$). (a) Apatite-in-olivine isomekes show that the thermobarometer has a moderate T dependence, wide isomeke spacing (changing P_{inc} by 100 MPa changes P_{trap} by ~1 GPa), and apatite inclusions primarily preserve compression at geologic conditions (tension at low P_{trap}), (d) P_{trap} has a significant X_{fa} dependence at high P_{inc} ($T_{trap} = 500^{\circ}$ C), and (g) T_{trap} has a moderate X_{fa} dependence ($P_{trap} = 1$ GPa). (b) Rutile-in-garnet isomekes show that the thermobarometer has a moderate T dependence, wide isomeke spacing (changing P_{inc} by 100 MPa changes P_{trap} by ~1 GPa), and rutile inclusions should preserve tension at geologic conditions; (e) P_{trap} has a significant X_{gr} dependence at low P_{inc} ($T_{trap} = 500^{\circ}$ C); and (h) T_{trap} has a moderate X_{gr} dependence ($P_{trap} = 1$ GPa). (c) Albite-in-epidote isomekes show that the barometer has a minimal T dependence, narrow isomeke spacing (changing P_{inc} by 100 MPa changes P_{trap} by ~0.25 GPa) and albite inclusions should preserve compression at geologic conditions; (f) P_{trap} has a moderate X_{ep} dependence at high P_{inc} , but its dependence on composition is minimal at low P_{trap} (P_{trap} = 500°C); and (i) because of the shallow isomekes of this barometer, P_{trap} shows an extreme P_{trap} dependence ($P_{trap} = 1$ GPa). Black solid lines indicate where $P_{inc} > 0$ (thin) and $P_{inc} = 0$ (thick). Dashed lines indicate $P_{inc} < 0$ isomekes. Gray areas highlight the P-T space where measured residual P_{inc} should retain tension ($P_{inc} < 0$).

slope indicates that the ap-in-ol thermobarometer is near the median of all tested pairs and that it could be appropriate as a barometer. The wide isomeke spacing indicates that this is a low sensitivity thermobarometer and that small changes in P_{inc} will cause large changes in calculated P_{trap} (Figure 1b).

For apatite in the $P6_3/m$ space group, group theory predicts the following Raman active vibrational modes (Kroumova et al., 2003):

$$\Gamma_{raman} = 12A_g + 16E_{1g} + 26E_{2g}$$

A total of 54 vibrational modes are Raman active, but only a few modes have sufficient intensity to be observed in the Raman spectra of randomly oriented apatite (Comodi et al., 2001). We focus on the \sim 964 cm $^{-1}$ band of apatite inclusions because of the strong intensity of this band (Figures 2a, 3a, and

CISNEROS AND BEFUS 9 of 21

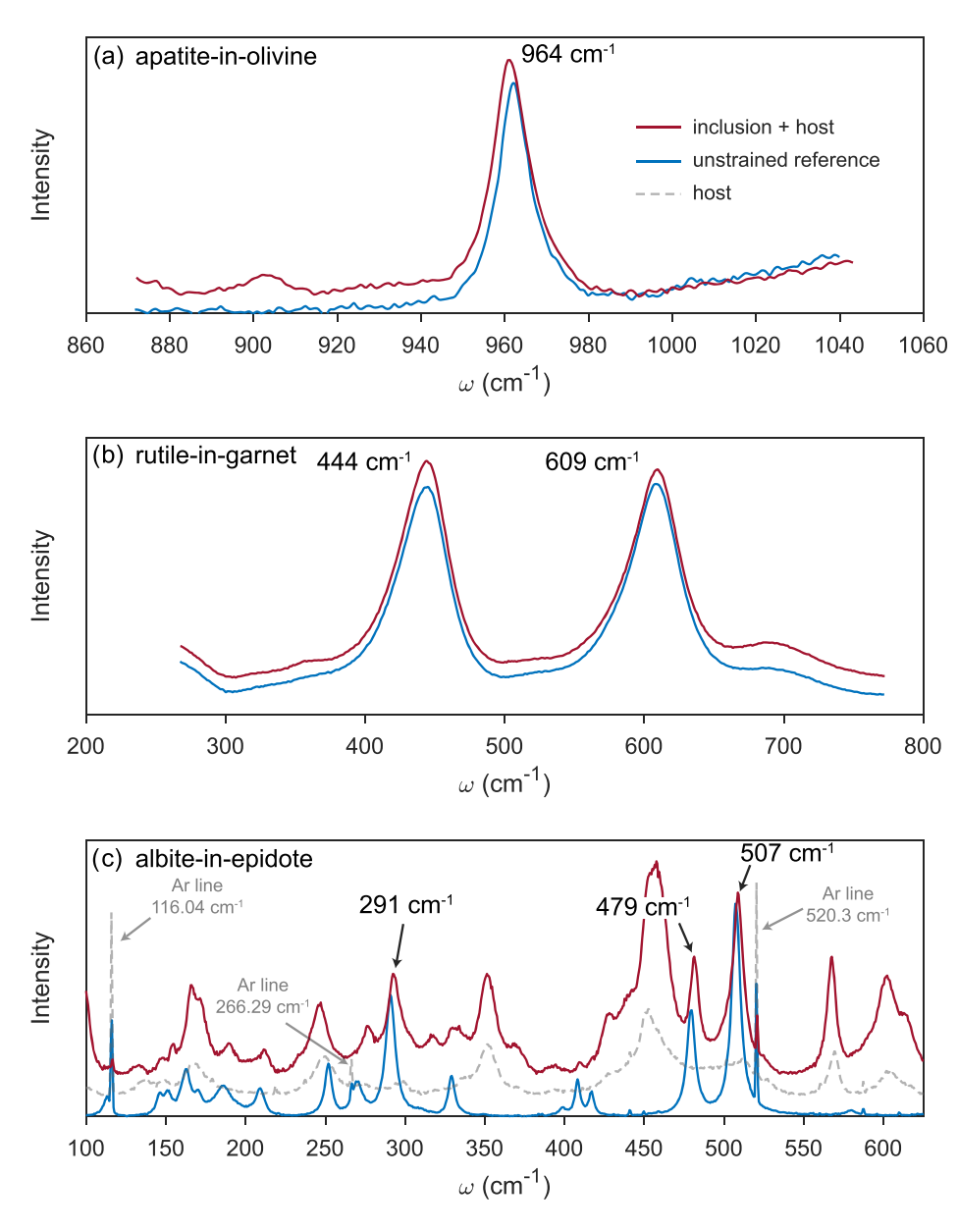


Figure 3. Raman spectra of (a) apatite inclusions in olivine, (b) rutile inclusions in garnet, and (c) albite inclusions in epidote. Red, blue, and dotted gray lines are the Raman spectra of the inclusion and host, unstrained inclusion, and host (only epidote shown), respectively.

4a). Raman intensities of other apatite bands were too low to peak fit. The prominent ~964 cm⁻¹ band represents the phosphate symmetric stretch ($\nu_1[A_g]$; Comodi et al., 2001). No overlap was observed between apatite and olivine Raman bands, and the Raman spectra of apatite inclusions required no deconvolution of shoulder bands near 964 cm⁻¹ (Figure 3a). Neighboring apatite peaks at ~950 and 1,030 cm⁻¹ represent distortion of the symmetric stretching mode owing to radiation damage, and the asymmetric stretch of the $\nu_{3b}(E_{2g})$ mode, respectively (Comodi et al., 2001; J. Liu et al., 2008). We postulate that the measured apatite inclusions have negligible radiation damage and are appropriate to use for this study, because of the relatively young age (< ~100 ka) of the Solfatara Plateau Lava flow and the low intensity of the ~950 cm⁻¹ band (Figure 3a). Separated apatite grains have mean peak positions at 962.3 \pm 0.1 cm⁻¹ (n = 4, s.d. of measurements), whereas apatite inclusions in olivine have

CISNEROS AND BEFUS 10 of 21

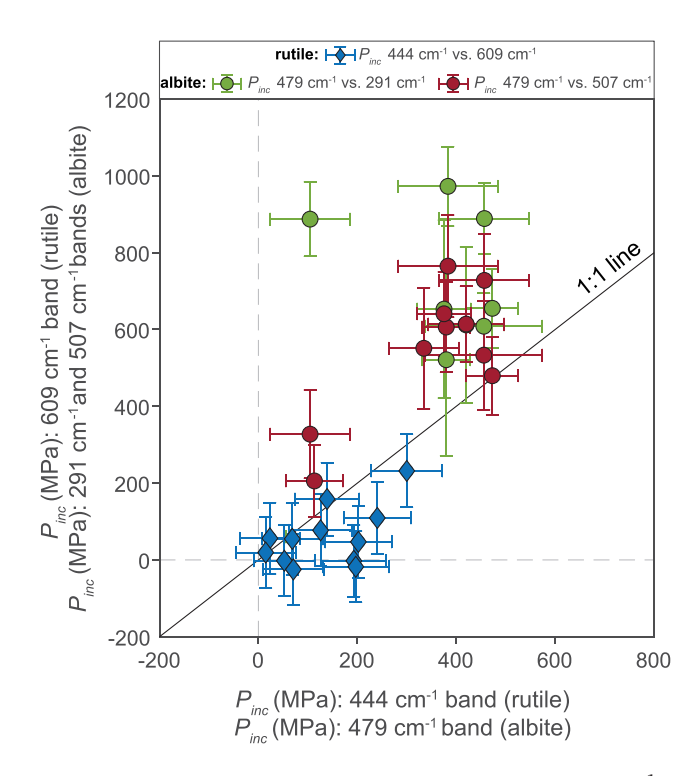


Figure 4. Comparison of P_{inc} calculated from the rutile 444 and 609 cm⁻¹ bands (blue), and the albite 279, 479, and 507 cm⁻¹ bands (red). The solid black line shows where P_{inc} calculated from different bands would have the same values (1:1 line, hydrostatic stress). For rutile inclusions, P_{inc} calculated from both bands center around the 1:1 line and cluster around $P_{inc} = 0$ (unstrained). For albite inclusions, P_{inc} calculated from the 279 and 509 cm⁻¹ bands generally exceed P_{inc} calculated from the 479 cm⁻¹ band. The s.d. of P_{inc} calculated from the 479 cm⁻¹ band (s.d. around mean) is also less and clusters around 400 MPa.

mean peaks at 961.7 \pm 0.4 cm⁻¹ (n=10) (Table 2). The enclosed apatite inclusions primarily exist under tension, as demonstrated by the mean negative peak shift of apatite inclusions relative to apatite in the matrix ($\Delta\omega = -0.6 \pm 0.4$ cm⁻¹).

The apatite 964 cm⁻¹ band exhibits a pressure-dependent Raman shift that has been experimentally calibrated under hydrostatic conditions (Comodi et al., 2001; Schouwink et al., 2010). We calculate residual pressures by using the P- $\Delta\omega$ relationship for fluoroapatite given in Ashley et al. (2017). Additional error may be introduced by using a P- $\Delta\omega$ relationship derived from Durango fluoroapatite, but the difference in composition between the Durango apatite used for hydrostatic experiments ($X_F = 0.99$) and our measured apatites ($X_F = 0.91$) is minimal (Schouwink et al., 2010). The calculated mean residual P_{inc} and s.d. recorded by apatite is -141 ± 96 MPa (n = 10), suggesting that these inclusions preserve tension (Table 2).

3.2.2. Rutile-in-Garnet: A Metamorphic Application

Metamorphic petrology is fundamental for understanding crustal and mantle dynamics, with processes that include continent and oceanic lithosphere subduction, obduction and exhumation, crustal strength, fault mechanics and rheology, and the effects of mantle dynamics on the evolution of the crust. A key approach used for understanding these problems is constraining the P-T evolution of metamorphic rocks from these different environments. A large number of metamorphic rocks have suitable thermobarometers; nonetheless, P-T conditions are difficult to extract from some common rock types (e.g., retrogressed metamorphic rocks, eclogites, skarn deposits, and spinel-bearing peridotites). Elastic thermobarometry offers great promise for metamorphic rocks and can potentially be used to constrain P-T conditions of distinct mineral growth.

For our second case study, we examine rutile inclusions in garnet (ruin-grt) from the Verpeneset eclogite in western Norway (Figures 2b, 3b, and 4b). Eclogites near Verpeneset in western Norway outcrop within ~400 Ma gneisses formed during the Caledonian Orogeny (Carswell et al., 2003; Kylander-Clark et al., 2008; Tsujimori et al., 2006; Wain et al., 2000) and record peak metamorphic conditions of ~2.5 \pm 0.3 GPa and 676 \pm 88°C (Carswell et al., 2003; Hacker et al., 2010; Wain et al., 2000) The eclogite contains a peak metamorphic assemblage of omphacite + garnet + zoisite (interpreted as pseudomorphs after lawsonite) + kyanite + rutile \pm talc \pm phengite \pm coesite (interpreted from polycrystalline quartz aggregates) with retrograde hornblende + quartz (Krogh, 1982; Wain et al., 2000). The garnets are compositionally zoned; thus, we restricted Raman analyses of rutile to near the core to limit compositional effects. Garnet core compositions are $Pyp_{24-35}Alm_{40-43}Grs_{20-25}Sps_{0-10}$ (Krogh, 1982).

Elastic modeling shows that for ru-in-grt, over the window of $T_{trap} = 500^{\circ}\text{C}$ to 900°C and $P_{inc} = 200$ MPa: $\kappa = 5^{\circ}$, $dP/dT \approx -3.8$ MPa °C⁻¹ (Figures 1a and 1c), and between the -400 and -300 MPa P_{inc} isomekes at $T_{trap} = 500^{\circ}\text{C}$, spacing ≈ 310 (Figure 1d). The isomeke slope indicates that the ru-in-grt thermobarometer is above the median dP/dT of all tested pairs and that it requires a good independent temperature constraint. Furthermore, the wide isomeke spacing indicates that this is a low sensitivity thermobarometer and that small changes in P_{inc} will cause large changes in P_{trap} (Figure 1b).

For rutile in the $P4_2/mnm$ space group, group theory predicts the following Raman active vibrational modes (Kroumova et al., 2003):

$$\Gamma_{raman} = A_{1g} + B_{1g} + B_{2g} + E_{g}.$$

The E_g and $A1_g$ vibrational modes can be well observed in the Raman spectra as broad bands at ~444 and ~609 cm⁻¹, respectively (Figures 3b; e.g., Balachandran & Eror, 1982). Additional Raman bands at ~145 and ~826 cm⁻¹ have been assigned to B_{1g} and B_{2g} modes, respectively (Frank et al., 2012), and a broad

CISNEROS AND BEFUS 11 of 21



band observed at ~235 cm⁻¹ has not been predicted by theoretical calculations. We focus on the intense ~444 and ~609 cm⁻¹ bands (Figure 3b). No overlap was observed between rutile and garnet Raman bands, but the Raman spectra of rutile inclusions required deconvolution of ~2–3 shoulder bands near both the 444 and 609 cm⁻¹ bands, suggesting that these bands result from multiphonon modes (see supporting information). Separated rutile grains have mean peak positions at 443.3 \pm 0.7 and 609.2 \pm 0.3 cm⁻¹ (n = 5), whereas fully encapsulated rutile inclusions have average peak positions at 444.2 \pm 0.6 and 609.5 \pm 0.3 cm⁻¹ (n = 12) (Table 2). We use the hydrostatic experiments of Liu and Mernagh (1992) that demonstrate that both rutile bands experience pressure-dependent Raman shifts to higher wave numbers and regress their rutile data to determine P- $\Delta\omega$ relationships (Figure S4; Table S4). The mean P_{inc} and s.d. calculated from the ~444 and ~609 cm⁻¹ rutile bands are 135 \pm 92 and 59 \pm 77 MPa (n = 12), respectively (Figure 4).

3.2.3. Feldspar-in-Epidote: A Second Metamorphic Application

Our final case study examines the potential of albite inclusions in epidote (ab-in-ep). The high β (low K) of feldspar and its widespread occurrence in diverse geologic settings make it a promising inclusion that can be used as barometer in many host phases (Figures 1 and 2c). We focus on testing the ab-in-ep barometer because epidote is a "stiff" host and is abundant in many mafic and felsic metamorphic rocks. Albite and epidote are also common in a wide variety of hydrothermal systems, and the ab-in-ep barometer can be useful for constraining pressures of deep roots below porphyry deposits, where both minerals are commonly found as alteration products (e.g., Runyon et al., 2019).

We analyze a mafic blueschist from the high-P/low-T Cycladic Blueschist Unit (Kalamisia Beach: 37°25' 12.2"N, 024°57′23.9"E) on Syros, Greece (Figures 2c, 3c, and 4c) to test the ab-in-ep barometer. The metamorphic complex exposed on Syros reached max P-T conditions of ~1.5-2.2 GPa and ~500-550°C at ~50 Ma (e.g., Laurent et al., 2018; Schumacher et al., 2008). It was subsequently exhumed to the midcrust by the Miocene with episodes of deformation and retrogression during exhumation prior to and post-core complex capture (Bröcker & Enders, 1999; Putlitz et al., 2005; Soukis & Stockli, 2013). Our sample is composed of an assemblage of garnet + omphacite + glaucophane + epidote + phengite + albite + quartz + chlorite (Figure S6). The primary external foliation is defined by omphacite, glaucophane, epidote, and white mica. Garnets are rotated by the primary foliation and often contain glaucophane growth within pressure shadows and brittle garnet fractures but do not have a well-developed internal foliation, suggesting that the primary foliation formed after garnet growth. Omphacite displays alteration and breakdown to glaucophane, and glaucophane and other inclusions within epidote are commonly oriented parallel to the external foliation. No omphacite is observed as inclusions within epidote. Therefore, our observations suggest that epidote crystallization occurred during retrograde metamorphism and garnet grew during earlier high-P metamorphism. Elastic modeling shows that for ab-in-ep, over the window of $T_{trap} = 500$ to 900°C and $P_{inc} = 200$ MPa: $\kappa = 0.2^{\circ}$, $dP/dT \approx -0.05$ MPa°C⁻¹ (Figures 1a and 1c), and between the 100 and 200 MPa P_{inc} isomekes at $T_{trap} = 500$ °C, spacing ≈ 250 (Figure 1d). The isomeke slope indicates that the ab-in-ep barometer is well below the 16th percentile of all tested pairs (0.5 MPa °C⁻¹) and that theoretically, it is an excellent barometer. The barometer has isomeke spacing above the median of all pairs (193) but is more sensitive than the ap-in-ol and ru-in-grt thermobarometers (Figures 1b and 2c).

For albite in the *P*-1 space group, group theory predicts the following Raman active vibrational modes (Kroumova et al., 2003):

$$\Gamma_{raman} = 39A_g$$

All 39 vibrational modes can be observed in the Raman spectra (Aliatis et al., 2015; McKeown, 2005), but we calculate a residual P_{inc} by using the high-intensity ~291 cm⁻¹ (ν_{14}), ~479 cm⁻¹ (ν_{22}), and ~507 cm⁻¹ (ν_{24}) bands of albite inclusions (Figure 3c). The ν_{14} , and ν_{22} and ν_{24} vibrational modes of albite represent rotation-translation, stretching, bending, and "breathing" of four-membered rings of Si (Al)-O-Si (Al), respectively (e.g., Freeman et al., 2008; McKeown, 2005). Specifically, ν_{14} , ν_{22} , and ν_{24} modes reflect tetrahedral cage shear within the ac-plane, tetrahedral ring compression in the ab-plane (Na-coordination expansion, Na-O stretch), and compression in the c-plane (Na-coordination expansion, O-Na-O breathing), respectively (McKeown, 2005). Extensive overlap was observed between albite and epidote Raman bands, and peak fitting of albite bands required significant peak deconvolution (see the supporting information).

CISNEROS AND BEFUS 12 of 21



Albite inclusions preserve Raman shifts ($\Delta\omega$) to higher wavenumbers (+0.4 to +2.1 cm⁻¹). We use the hydrostatic experiments of Befus et al. (2018), which demonstrate that all albite bands experience pressure-dependent Raman shifts to higher wave numbers and regress their albite data to determine $P-\Delta\omega$ relationships (Figure S4; Table S4). The mean P_{inc} and s.d. calculated from the albite 291, 479, and 507 cm⁻¹ bands are 725 \pm 166 MPa (n=8), 376 \pm 112 MPa (n=9), and 583 \pm 132 MPa (n=9), respectively (Figure 4; Table 2).

4. Discussion

Our results suggest that many untested inclusion-host pairs from diverse geologic environments have the potential to be used in elastic thermobarometry (Table 3). To test some of the newly modeled inclusion-host pairs, we provide three case studies that use samples with reference magmatic and metamorphic P-T constraints. We show that mechanical, theoretical, and analytical limitations, and/or inaccurate thermodynamic properties, may sometimes restrict the utility of elastic thermobarometry.

4.1. Isomeke Slope and Spacing

Previous work has shown that isomeke slopes are related to the difference between the K and α of an inclusion-host pair (Equation 3; Angel et al., 2015; Kohn, 2014). We similarly find that inclusions with high β (e.g., low K phases such as quartz, feldspar, apatites, amphiboles, graphite, and micas) serve as the best barometers, and inclusions-host pairs with large K differences are the best barometers. Inclusion-host pairs that have similar K, but a significant difference in α , serve as the best thermometers (e.g., zircon-in-garnet, zircon-in-rutile, and garnet-in-olivine). Similar to elastic thermometers, isomeke spacing is related to the difference of K between an inclusion and host. Inclusion-host pairs with small and large K differences will have large and small isomeke spacing, respectively.

Isomeke slope and spacing demonstrate the P-T dependence of the inclusion-host pair, and the sensitivity of the pair to changes in P_{inc} , respectively. The useful range of each variable will depend on the application of interest. For example, quartz-in-almandine isomekes have a slope of ~1.8 MPa °C⁻¹, near the median slope of 1.9 MPa °C⁻¹, and far above the arbitrary 16th percentile slope threshold of 0.5 MPa °C⁻¹ (Figure 1c); however, quartz-in-garnet is known to be a reliable barometer (e.g., Ashley et al., 2014; Bonazzi et al., 2019; Thomas & Spear, 2018; Wolfe & Spear, 2018). Large isomeke spacing (\geq ~300) may make using some inclusion-host pairs (e.g., rutile-in-garnet) to constrain P-T conditions of crustal processes challenging. Inclusion-host pairs can also be sensitive to mineral and host compositions, affecting their theromobarometry potential. Table 3 demonstrates how different solid-solution compositions can change the isomeke slope and spacing; thus, the compositional sensitivity of inclusion-host pairs should be evaluated for reasonable geologic compositions.

4.2. Current Limitations of Elastic Thermobarometry and Calculations in This Study

We emphasize that our theoretical calculations (isomeke slope and spacing) and associated inclusion-host pair case study calculations (sections 4.3–4.5) have several limitations. Isomeke slope and spacing should be carefully evaluated for each inclusion-host pair of interest. At geologically relevant temperatures, nonlinear isomekes may become increasingly important for minerals that undergo phase transitions, and this may also limit the applicability of our spacing calculations that assume linear isomekes. We describe two other major limitations of our case-study calculations in this work: strain resolvability and inclusion-host anisotropy. We refer to strain resolvability as uncertainties associated with P-V-T data, and the $\Delta\omega$ precision required to provide reasonable P_{trap} errors.

Elastic thermobarometry requires careful evaluation of mineral thermodynamic properties and may require refitting P-V-T data with appropriate EoS. Implementing thermodynamic properties from large thermodynamic databases (e.g., Holland & Powell, 2011) should be approached with caution. In this work, we implement refit P-V-T data for apatite, rutile, garnet, and epidote; however, olivine and albite thermodynamic properties are derived from the Holland and Powell (2011) database and may require further evaluation. As further discussed in sections 4.3 and 4.4, for inclusion-host pairs such as apatite-in-olivine and rutile-in-garnet, $\Delta\omega$ errors must be small because these inclusion-host pairs have large isomeke spacing. $\Delta\omega$ errors will increase P_{inc} errors (calculated using Grüneisen tensors or hydrostatic calibrations) and resultant P_{trap}

CISNEROS AND BEFUS 13 of 21

H H H H

Environment	Inclusion-host pair	Slope (MPa °C ⁻¹)	P-T potential	Spacing ^a	P _{inc} range (MPa) ^b	Stress state
Mantle	Pyroxene-in-diamond	2.0 to 3.2	Thermobarometer	45 to 70	-1,000 to 3,000	Tension to compression
	OPX (En90Hed10)	2.1	Thermobarometer	99	-1,000 to 3,000	Tension to compression
	Diopside	3.2	Thermobarometer	48	-1,000 to 3,000	Tension to compression
	Garnet-in-diamondd	2.0 to 4.9	Thermobarometer	38 to 77	-2,000 to 1,000	Tension to compression
	Pyrope (Pv80Alm15Gr5)	4.2	Thermobarometer	48	-2,000 to 1,000	Tension to compression
Igneous	Magnetite-in-olivine (Fo100)	2.5	Thermobarometer	196	-1,000 to -600	Tension
	Feldspar-in-pyroxene	0 to 7.9	Thermobarometer	0.4 to 300	100 to 2,000	Compression
	Andesine (An40Ab60)-in-augite (Di50En50)	1.5	Barometer	210	200 to 1,200	Compression
	Feldspar-in-olivine	0.4 to 5.2	Thermobarometer	90 to 295	100 to 5,000	Compression
	Anorthite (An90Ab10)-in-forsterite (F092)	3.6	Thermobarometer	110	400 to 1,500	Compression
	Sanidine (Or50Ab45An5)-in-fayalite (Fa90)	1.0	Barometer	220	200 to 1,000	Compression
	Apatite-in-zircon ^c	3.2	Thermobarometer	06	-1,000 to -500	Tension
Skarn and Hydrothermal	Calcite-in-garnet	0.2 to 1.4	Barometer	150 to 295	-500 to $1,500$	Tension to compression
	Andradite (And60Grs40)	0.5	Barometer	230	-50 to $1,500$	Tension to compression
	Rutile-in-quartz	2.4	Thermobarometer	30	-1,000 to 1,000	Tension to compression
	Apatite-in-garnet	0.1 to 3.3	Thermobarometer	125 to 310	-500 to $1,500$	Tension to compression
	Fluoroapatite(F75OH25)-in-andradite (And90Grs10)	0.9	Barometer	290	-200 to 1,500	Tension to compression
	Wollastonite-in-epidote	0.3	Barometer	460	0 to 1,000	Compression
Metamorphic (range of facies)	Plagioclase-in-garnet	0 to 3.8	Thermobarometer	90 to 230	0 to 2,000	Compression
	Andesine (An40Ab60)-in-almandine (Alm75Py15Grs10)	0.2	Barometer	210	0 to 2,000	Compression
	Aluminosilicates-in-garnet	0.8 to 20	Thermobarometer	5 to 2,200	0 to 500	Compression
	Kyanite-in-almandine (Alm60Py20Grs20)	0 to 0.4	Barometer	2000	0 to 500	Compression
	Ilmenite-in-andalusite	11.4	Thermometer	120	-400 to -200	Tension
	Calcite-in-corundum	1.2	Barometer	145	-700 to 300	Tension to compression
	Amphibole-in-garnet	0.8-1.2	Barometer	250	100 to 700	Compression
	Riebeckite-in-almandine (Alm75Py15Grs10)	0.8	Barometer	248	300 to 700	Compression
	Glaucophane-in-almandine (Alm75Py15Grs10)	1.2	Barometer	311	400 to 700	Compression
	Magnetite-in-clinozoisite	1.7	Thermobarometer	140	-2,000 to -500	Tension

Note. Ranges are provided for mineral pairs to encompass compositional endmembers. Results for specific solid solutions are shown for some realistic pairs. Isomeke slope and spacing provide insight into a thermobarometers potential and sensitivity. Pinc range provides the theoretical range of pressures an inclusion should preserve at ambient conditions, if it records reasonable geo-

logic P-T conditions.

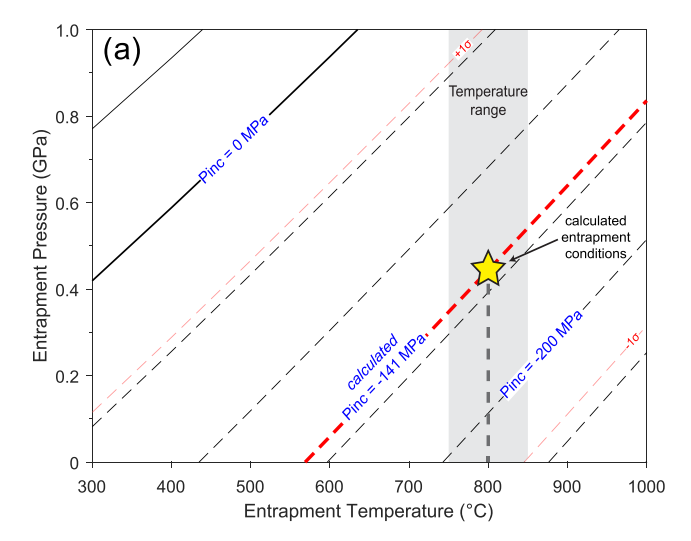
^aSpacing is measured perpendicular to the slope of the isomeke, and measured as the difference between 100 MPa isomekes.

^bIt is unclear if high magnitudes of tension can be preserved in inclusions. Values as high as these may be unlikely.

^cApatite is a common inclusion, generally exists under tension at ambient conditions, and is typically a thermometer. Radioactivity may soften apatite and/or zircon.

^cAse Izraeli et al. (1999) for further applications of inclusions in diamond.

CISNEROS AND BEFUS 14 of 21



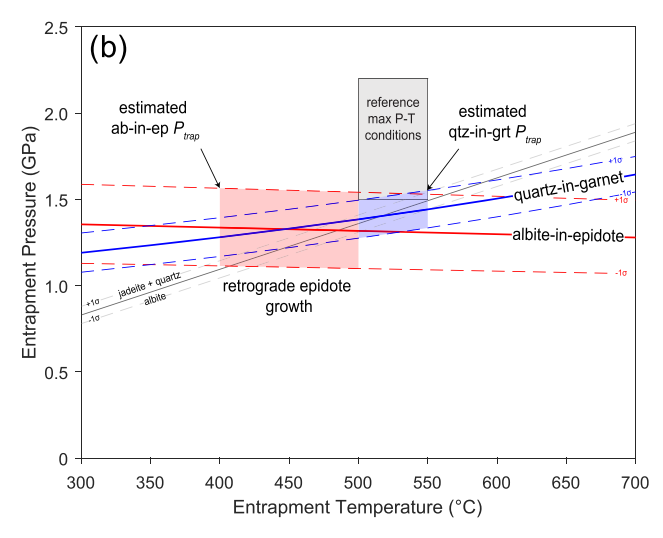


Figure 5. Entrapment pressure estimates from two case studies. (a) Apatite-in-olivine results (yellow star) suggest a higher P_{trap} than previously published reference P-T conditions (gray box); however, uncertainties are large for these calculations. The thick red dashed line is our calculated residual P_{inc} , and thin red dashed lines represent the 1σ P_{inc} error. Apatite and olivine modeled as $X_{ap\text{-}fluoro}=0.91$, $X_{ap\text{-}hydroxyl}=0.05$, $X_{ap\text{-}chloro}=0.04$, and $X_{fa}=0.92$, $X_{fo}=0.08$, respectively. (b) Albite-in-epidote P_{trap} isomeke (solid red) relative to the quartz-in-garnet P_{trap} isomeke (solid blue), previously determined maximum P-T conditions (gray box), and the jadeite + quartz to albite reaction line (solid gray). Ab-in-ep and qtz-in-ep P_{trap} isomekes are calculated from the weighted mean P_{inc} of all analyses (Tables 2 and S6). Dashed red, blue, and gray lines bracket the 1σ error of P_{trap} and the reaction line. Felspar and epidote modeled as $X_{ab}=1$, and $X_{ep}=0.5$, $X_{cz}=0.5$, respectively. Quartz and garnet modeled as $X_{qtz}=1$, and $X_{alm}=0.7$, $X_{grs}=0.2$, and $X_{prp}=0.1$, respectively.

errors. $\Delta\omega$ errors can be reduced by using high spectral resolution Raman systems, appropriate spectral calibrations, and many repeat measurements.

The effect of inclusion and host mineral anisotropy (different compressibility and thermal expansivity along different crystallographic axes) on elastic thermobarometry calculations is an issue that has been addressed by recent studies (e.g., Angel et al., 2019; Murri et al., 2018). Recent work has shown that using hydrostatic stress calibrations to constrain quartz inclusion pressures may sometimes lead to inaccurate estimates of garnet growth conditions (3.0 GPa experiments); however, at lower pressures (2.5 GPa experiments), hydrostatic calibrations replicate known pressure conditions of garnet growth (Bonazzi et al., 2019). Furthermore, previous experimental studies suggest that calculating quartz P_{incl} by using hydrostatic calibrations produces accurate P_{trap} estimates of garnet growth (Thomas & Spear, 2018). The current limitations of using hydrostatic calibrations to calculate P_{trap} remain unclear and certainly require further experimental testing. We reiterate that our case studies use hydrostatic calibrations to constrain residual pressures of apatite, rutile, and albite inclusions and that we do not account for anisotropy. Therefore, the inclusion-host pairs in our case studies require further evaluation before any pairs can be implemented for accurate P_{trap} calculations. Furthermore, the accuracy of modeling anisotropic minerals with an isotropic elastic model remains unknown, though recent results suggest that an isotropic elastic model satisfactorily simulates the P_{inc} evolution of an anisotropic inclusion-host pair during isobaric heating (quartz inclusions in epidote; Cisneros et al., 2020).

4.3. Apatite-in-Olivine: An Igneous Rock Application

Apatite inclusions from the Solfatara Plateau, Yellowstone caldera, preserve tension, with a mean residual $P_{inc}=-141\pm96$ MPa $(n=10, {\rm Table~2})$, calculated from the apatite 964 cm $^{-1}$ band. The s. d. around the mean residual P_{inc} is large and may result from inclusion and/or host anisotropy that we have not accounted for, apatite shape effects, or differences in compositions between inclusion and matrix grains. To calculate P_{trap} , we estimate apatite compositions by using empirical volatile relationships to be $X_{Cl}=0.04, X_F=0.91$, and $X_{OH}=0.05$ (see the supporting information). The pre-eruptive magmatic temperature (T_{trap}) and olivine composition of Solfatara Plateau are $800\pm50^{\circ}{\rm C}$ and ${\rm Fa_{92~\pm~1}}$ (Befus & Gardner, 2016; Vazquez et al., 2009).

We calculate that Solfatara Plateau apatite inclusions were entrapped by olivine at $\sim 0.44 \pm 0.57$ GPa using mean mineral compositions and our mean residual P_{inc} (Figure 5a). Our best estimate P_{trap}

(~0.44 GPa) suggests crystallization in a deep crustal reservoir that is deeper than independent estimates for rhyolitic storage at Yellowstone caldera, but our uncertainty overlaps with reference conditions (Befus & Gardner, 2016; Gryger, 2017; Luttrell et al., 2013; Myers et al., 2016; Shamloo & Till, 2019). We attribute the discrepancy to significant limitations with the ap-in-ol thermobarometer. P_{trap} estimates from the thermobarometer vary considerably as a function of olivine composition; this effect becomes more pronounced at higher residual P_{inc} (e.g., 800 MPa; Figure 2d). At lower residual P_{inc} (e.g., -100 MPa), the effect of olivine composition on the resultant P_{trap} is smaller, but nonnegligible. Given our estimated isomeke slope of the ap-in-ol thermobarometer $(dP/dT \approx 1.7 \text{ MPa} ^{\circ}\text{C}^{-1})$, changes in T_{trap} should have an effect on the final

CISNEROS AND BEFUS 15 of 21



 P_{trap} , for example, changing T_{trap} by 50°C changes P_{trap} by \pm 0.1 GPa. A further limitation associated with the ap-in-ol thermobarometer is the isomeke spacing (~280). The average P_{inc} error of our individual inclusion measurements (\pm 65 MPa) would change the final P_{trap} by \pm 0.4 GPa (Figures 2a and 5a). Raman system uncertainties of ~0.1 cm⁻¹ can reduce P_{inc} errors to ~34 MPa ($P_{trap} \pm$ 0.2 GPa), but even \pm 0.2 GPa errors may not be appropriate for many applications when compounded with other uncertainties (e.g., T_{trap} , mineral compositions, shape effects, softening of apatite from radiation damage, and anisotropy). In principle, the ap-in-ol thermobarometer can have wide-ranging applications for constraining pressures of magmatic systems but will require accurate constraints on all input variables, low instrumental uncertainties, or many repeat measurements.

4.4. Rutile-in-Garnet: A Metamorphic Application

The mean residual P_{inc} calculated from the rutile 444 and 609 cm⁻¹ bands are 135 ± 92 MPa and 59 ± 77 MPa (n=12), respectively. Individual rutile inclusion analyses provide similar P_{inc} from both rutile bands, and most inclusion analyses center near $P_{inc} = 0$ (within error; Figure 4). Using our mean residual P_{inc} , $T_{trap} = 676$ °C, and a $Pyp_3Alm_{40}Grs_{20}Sps_{10}$ garnet core composition, we calculate that rutile inclusions from Verpeneset eclogites were entrapped by garnet at negative pressures. Cleary, these results are unrealistic and do not represent known geologic conditions of garnet growth and reference pressure estimates. The errant result can be sourced back to the calculated residual P_{inc} from all analyses. Rutile inclusions should preserve negative pressures (tension) at Earth conditions, and high negative residual pressures at reference conditions (~ -300 MPa; Figure 2b) (Zaffiro et al., 2019).

Several possible processes can explain the low P_{trap} that the ru-in-grt thermobarometer records. During exhumation, rutile inclusions may have in-elastically relaxed next to the garnet exterior or fractures, thus reducing residual pressures; however, in accordance with Mazzucchelli et al. (2018), the rutile inclusions were small relative to the garnet host, and sufficiently far away from the garnet exterior and fractures to avoid relaxation. Proximity to adjacent inclusions would produce higher inclusion pressures relative to those predicted by pure elastic relaxation; therefore, this possibility is also unlikely. Rutile inclusions are generally elongate and anisotropic crystals; therefore, elastic modeling of rutile inclusions as isotropic, spherical minerals may be inappropriate. Furthermore, radiation damage may lead to significant softening of rutile (decrease of K), and an *increase* of P_{inc} , as we observe in our samples (lower P_{trap} ; e.g., Beirau et al., 2016). Significant radiation damage is plausible, given the ~400 Ma age of eclogite facies metamorphism in the Western Gneiss Region (Carswell et al., 2003). Additionally, tensile failure of the host may cause collapse around rutile inclusions, and an *increase* of P_{inc} .

The preceding issues are plausible, especially for rutile inclusions that record positive residual P_{inc} , but two of the primary issues that may limit ru-in-grt and other thermobarometers are the nature of rutile Raman bands, and that inclusions may not be able to retain ideal tensile strains at geologically relevant conditions. First, we find that peak positions of rutile Raman bands are extremely sensitive to the peak fitting approach that is implemented. The rutile Raman bands are broad, and the peak center position is challenging to constrain. Rutile Raman bands also exhibit varying degrees of asymmetry (especially the ~444 cm⁻¹ band), and we find that symmetric peak fitting functions did not adequately fit rutile bands (Figure S2). Variable peak fitting approaches (e.g., symmetric vs. nonsymmetric distributions) can produce changes in peak center positions near ~2 cm⁻¹. Second, isomekes for this thermobarometer are inverted; that is, lower residual pressures indicate higher pressures of entrapment (Figure 2b). If rutile inclusions are entrapped at high pressures, they may not be able to retain sufficient adhesion to the surrounding host cavity wall and therefore do not preserve an ideal tensional strain state. Similarly, apatite inclusionsinolivine may preserve a high P_{inc} (~ -140 MPa) relative to their ideal P_{inc} (~ -200 MPa) and may also suggest a tensile strain limit to elastic thermobarometry. For comparison, quartz inclusions in garnet have been shown to retain some tension (Ashley et al., 2015) and in some cases may preserve sufficient tension to give accurate pressures estimates (0.8 GPa experiments; $P_{inc} = -300$ MPa; Thomas & Spear, 2018). The difference in result between previous studies and ours is problematic, given that the residual P_{inc} required from both thermobarometers to replicate reference or experimental conditions is similar ($P_{inc} \approx -300$ MPa). The higher K of rutile relative to quartz ($K_{ru} = 205.1 \text{ GPa}$; $K_{qtz} = 64.3 \text{ GPa}$) may limit the amount of tension that rutile inclusions can accommodate and does not allow rutile to "stretch" to its ideal strain state. If so, this would imply that

CISNEROS AND BEFUS 16 of 21



inclusions that should retain negative residual P_{inc} at geologically relevant conditions but have a high $K_{inlcusion}$ may not efficiently attach to the host cavity and thus limits their applicability as elastic thermobarometers.

The ru-in-grt thermobarometer is further complicated by issues that are illustrated by associated isomekes. P_{trap} estimates from the thermobarometer can vary considerably as a function of garnet composition, and this effect becomes more pronounced at lower residual P_{inc} (e.g., -800 MPa; Figure 2e). Given our estimated isomeke slope of the ru-in-grt thermobarometer $(dP/dT\approx-3.8$ MPa °C⁻¹), changes in T_{trap} should affect the final P_{trap} , that is, changing T_{trap} by 50°C changes P_{trap} by \pm ~0.2 GPa. An additional limitation with the rutile-in-garnet barometer is isomeke spacing (~310). Assuming a garnet composition of $X_{gr}=1$, $T_{trap}=600$ °C, and $P_{inc}=-300$ MPa ($P_{trap}=1.72$ GPa), the average P_{inc} error of our individual inclusion measurements (\pm 88 MPa) would change the final P_{trap} by \pm ~1.1 GPa (Figure 2b). Cleary, future application of the rutile-in-garnet thermobarometer may be challenging, and successful application of this thermobarometer would require low uncertainty Raman measurements, and a better understanding of the tensile strain limit that inclusions can preserve.

4.5. Feldspar-in-Epidote: A Second Metamorphic Application

In comparison to the previous examples, we show an example that records a large, complicated range of residual P_{inc} , but reasonable P_{trap} conditions. The difference in P_{inc} calculated from the ~291 cm⁻¹ (ν_{14}), ~479 cm⁻¹ (ν_{22}), and ~507 cm⁻¹ (ν_{24}) feldspar bands suggests that our measured inclusions record significant anisotropy (Figure 4). P_{inc} calculated from the albite 291 and 507 cm⁻¹ bands generally record a higher P_{inc} than P_{inc} calculated from the albite 479 cm⁻¹ band. The ~291 cm⁻¹ band of albite generally records the highest P_{inc} . P_{inc} calculated from the ~479 cm⁻¹ is generally about 1.5–2 times less than P_{inc} calculated from the ~507 cm⁻¹ band (Figure 4; Table 2). The relationship may reflect the compression along two opposing feldspar axes, that is, tetrahedral ring compression in the ab-plane (ν_{22}) and compression in the c-plane (ν_{24}). To attempt to account for the significant P_{inc} variability that feldspars record, we calculate a weighted mean P_{inc} for each analysis. We assign a weight (ν) of

$$w_i = \frac{1}{\sigma_i^2},\tag{5}$$

where σ_i is the P_{inc} error calculated for each albite Raman band and w_i is the weight assigned to P_{inc} calculated from each band. We calculate a mean P_{inc} error based on the weighted variance of P_{inc} calculated from each band, relative to the mean P_{inc} of each analysis. This applies a lower mean P_{inc} error to samples that have a lower P_{inc} s.d., to apply more weight to albite analyses that exhibit less P_{inc} variability (Figure 4, closer to hydrostatic stress line). We calculate a weighted mean P_{inc} for the albite analyses population based on our previous weighting, to calculate a mean P_{trap} . We estimate the composition of the feldspar we analyzed to be pure albite (see the supporting information) and assume an epidote composition of X_{ep} 0.5, X_{cz} = 0.5.

To provide a comparison against P_{trap} calculated from the ab-in-ep barometer, we carried our qtz-in-grt measurements from the same thick section. To calculate P_{trap} from the qtz-in-grt barometer, we assume an ideal quartz and $Alm_{0.7}Grs_{0.2}Pyp_{0.1}$ garnet composition and account for quartz anisotropy by calculating our residual quartz P_{inc} from strains (Angel et al., 2019; Bonazzi et al., 2019; Murri et al., 2018). Further information about quartz P_{inc} calculations is provided in the supporting information. Between $T_{trap} = 500^{\circ}\text{C}$ and 550°C, using our mean P_{inc} (574 \pm 63 MPa), the qtz-in-grt barometer records P_{trap} between 1.38 to 1.44 GPa (Figure 5b; Tables S5 and S6). At $T_{trap} = 450^{\circ}\text{C}$, P_{trap} calculated from the ab-in-ep barometer is 1.3 \pm 0.2 GPa (Table 2). Changing T_{trap} from 400°C and 500°C only changes the mean P_{trap} from 1.34 to 1.32 GPa (Figure 5b). The P_{trap} we calculate from the qtz-in-grt and ab-in-ep barometers are consistent with high-P garnet growth near peak metamorphic conditions, and retrograde epidote growth at lower pressures. Our calculated ab-in-ep P_{trap} is also in reasonable agreement with the reaction Jadeite + Quartz to Albite (Figure 5b) (Holland, 1980).

The higher isomeke spacing sensitivity and shallow isomeke slope of the ap-in-ep barometer relative to the ap-in-ol and ru-in-grt thermobarometers significantly reduces P_{trap} errors; however, compounded

CISNEROS AND BEFUS 17 of 21



uncertainties may result from using albite P- $\Delta\omega$ calibrations and an unstrained Amelia albite standard, if the inclusion feldspar composition does not closely approximate albite. P_{trap} estimates also vary as a function of epidote composition, and this effect becomes more pronounced at higher residual P_{inc} (e.g., 800 MPa; Figure 2f). Given the estimated isomeke slope of the ab-in-ep barometer $(dP/dT \approx -0.05 \text{ MPa} \, ^{\circ}\text{C}^{-1})$, changes in T_{trap} have a negligible effect on the final P_{trap} . Changing T_{trap} by up to 700°C changes P_{trap} by less than 0.2 GPa. The ab-in-ep barometer has moderate isomeke spacing (~250). Assuming an epidote composition of $X_{ep} = 0.5$, $T_{trap} = 450$ °C, and $P_{inc} = 400 \text{ MPa}$ ($P_{trap} = 1.11 \text{ GPa}$), the population weighted mean P_{inc} error (\pm 76 MPa) would change the final P_{trap} by \pm ~0.2 GPa (Figure 2c and 5b). This preliminary work suggests that the ab-in-ep barometer may record reasonable P_{trap} conditions but that careful evaluation will be needed in the future to understand the effects of feldspar anisotropy and an anisotropic host. Synthesis experiments of albite inclusions that are entrapped by epidote at known conditions would be appropriate to test the accuracy of the barometer and hydrostatic calibrations (e.g., Bonazzi et al., 2019; Thomas & Spear, 2018). Furthermore, albite may be a more suitable inclusion in other host phases that exhibit less anisotropy than epidote (e.g., garnet).

5. Ongoing Directions

The purpose of this work is to present new inclusion-host pairs that have promising potential as elastic thermobarometers. Our contribution primarily presents the theoretical potential of inclusion-host pairs that can be used for elastic thermobarometry. We provide case studies to demonstrate inclusion-host pairs will present complexities that must be carefully considered.

We acknowledge that significant future work is needed to successfully implement the elastic thermobarometers that we present. Remaining work includes (but not limited to) better understanding the effects of anisotropy on residual P_{inc} , tensile strain limits, the limitations of 1-dimension elastic modeling, visco-elastic effects, and the effects of nonideal geometries; however, ongoing research is making progress with many of these issues (e.g., Mazzucchelli et al., 2018; Murri et al., 2018; Stangarone et al., 2019; Zhong et al., 2020). When the elastic properties and postentrapment modifications of inclusion-host pairs are carefully considered, the technique has far-reaching petrologic potential and could allow geoscientists to constrain P-T conditions of processes in diverse mantle, metamorphic, magmatic, and extraterrestrial settings.

Data Availability Statement

Files for the MATLAB program (https://doi.org/10.3929/ethz-b-000437754) and supporting information (https://www.research-collection.ethz.ch/handle/20.500.11850/437716) are archived in the ETH Zürich Research Collection data repository. Files for the MATLAB program are also available on GitHub (in the following repository: https://github.com/miguelcisneros/solid_inclusion_calculator_MATLAB).

References

- Adams, H. G., Cohen, L. H., & Rosenfeld, J. L. (1975a). Solid inclusion piezothermometry I: Comparison dilatometry. American Mineralogist, 60, 574–583.
- Adams, H. G., Cohen, L. H., & Rosenfeld, J. L. (1975b). Solid inclusion piezothermometry II: Geometric basis, calibration for the association quartz-garnet, and application to some pelitic schists. *American Mineralogist*, 60, 584–598.
- Aliatis, I., Lambruschi, E., Mantovani, L., Bersani, D., Andò, S., Gatta, G. D., et al. (2015). A comparison between ab initio calculated and measured Raman spectrum of triclinic albite (NaAlSi3O8). *Journal of Raman Spectroscopy*, 46(5), 501–508. https://doi.org/10.1002/jrs.4670
- Aliatis, I., Lambruschi, E., Mantovani, L., Bersani, D., Gatta, G. D., Tribaudino, M., & Lottici, P. P. (2017). High-pressure Raman spectroscopy on low albite. *Physics and Chemistry of Minerals*, 44(3), 213–220. https://doi.org/10.1007/s00269-016-0850-5
- Angel, R. J., Nimis, P., Mazzucchelli, M. L., Alvaro, M., & Nestola, F. (2015). How large are departures from lithostatic pressure? Constraints from host-inclusion elasticity. *Journal of Metamorphic Geology*, 33(8), 801–813. https://doi.org/10.1111/jmg.12138
- Angel, R. J., Alvaro, M., Miletich, R., & Nestola, F. (2017). A simple and generalised P-T-V EoS for continuous phase transitions, implemented in EosFit and applied to quartz. Contributions to Mineralogy and Petrology, 172(5), 29. https://doi.org/10.1007/s00410-017-1349-x
- Angel, R. J., Mazzucchelli, M. L., Alvaro, M., & Nestola, F. (2017). EosFit-Pinc: A simple GUI for host-inclusion elastic thermobarometry. American Mineralogist, 102(9), 1957–1960. https://doi.org/10.2138/am-2017-6190
- Angel, R. J., Mazzucchelli, M. L., Alvaro, M., Nimis, P., & Nestola, F. (2014). Geobarometry from host-inclusion systems: The role of elastic relaxation. *American Mineralogist*, 99(10), 2146–2149. https://doi.org/10.2138/am-2014-5047
- Angel, R. J., Murri, M., Mihailova, B., & Alvaro, M. (2019). Stress, strain and Raman shifts. Zeitschrift Für Kristallographie Crystalline Materials, 234(2), 129–140. https://doi.org/10.1515/zkri-2018-2112
- Asell, J. F., & Nicol, M. (1968). Raman spectrum of α quartz at high pressures. The Journal of Chemical Physics, 49(12), 5395–5399. https://doi.org/10.1063/1.1670064

Acknowledgments

We acknowledge NSF Grants EAR-1725110 (awarded to J. Barnes, W. Behr, and D. Stockli) and EAR-1724429 (awarded to K. B.) for financial support. Further appreciation is given to the Ford Foundation and the Geological Society of America for fellowship and grant financial support for M. C. Samples were collected under permit YELL-05678 and provided by the Smithsonian Institution. We thank M. MacInnis, M. Kohn, and an anonymous reviewer for helpful comments that greatly improved this manuscript. We thank T. Holland for help with modeling phases that undergo phase transitions and R. Angel, M. Alvaro, J. Barnes, and A. Lin for helpful discussions. We thank R. Bodnar and C. Farley at Virginia Tech for allowing us to use their Raman system.

CISNEROS AND BEFUS 18 of 21



- Ashley, K. T., Barkoff, D. W., & Steele-MacInnis, M. (2017). Barometric constraints based on apatite inclusions in garnet. *American Mineralogist*, 102(4), 743–749. https://doi.org/10.2138/am-2017-5898
- Ashley, K. T., Caddick, M. J., Steele-MacInnis, M. J., Bodnar, R. J., & Dragovic, B. (2014). Geothermobarometric history of subduction recorded by quartz inclusions in garnet. *Geochemistry, Geophysics, Geosystems*, 15, 350–360. https://doi.org/10.1002/2013GC005106
- Ashley, K. T., Darling, R. S., Bodnar, R. J., & Law, R. D. (2015). Significance of "stretched" mineral inclusions for reconstructing P-T exhumation history. Contributions to Mineralogy and Petrology, 169(6), 55. https://doi.org/10.1007/s00410-015-1149-0
- Ashley, K. T., Steele-MacInnis, M., Bodnar, R. J., & Darling, R. S. (2016). Quartz-in-garnet inclusion barometry under fire: Reducing uncertainty from model estimates. *Geology*, 44(9), 699–702. https://doi.org/10.1130/G38211.1
- Balachandran, U., & Eror, N. G. (1982). Raman spectra of titanium dioxide. Journal of Solid State Chemistry, 42(3), 276–282. https://doi.org/10.1016/0022-4596(82)90006-8
- Barkoff, D. W., Ashley, K. T., Silva, R. G. D., Mazdab, F. K., & Steele-MacInnis, M. (2019). Thermobarometry of three skarns in the Ludwig Area, Nevada, based on Raman spectroscopy and elastic modeling of mineral inclusions in garnet. *The Canadian Mineralogist*, 57(1), 25–45. https://doi.org/10.3749/canmin.1800050
- Barkoff, D. W., Ashley, K. T., & Steele-MacInnis, M. (2017). Pressures of skarn mineralization at Casting Copper, Nevada, USA, based on apatite inclusions in garnet. *Geology*, 45(10), 947–950. https://doi.org/10.1130/G39177.1
- Befus, K. S., & Gardner, J. E. (2016). Magma storage and evolution of the most recent effusive and explosive eruptions from Yellowstone Caldera. Contributions to Mineralogy and Petrology, 171(4), 30. https://doi.org/10.1007/s00410-016-1244-x
- Befus, K. S., Lin, J.-F., Cisneros, M., & Fu, S. (2018). Feldspar Raman shift and application as a magmatic thermobarometer. *American Mineralogist*, 103(4), 600–609. https://doi.org/10.2138/am-2018-6157
- Beirau, T., Nix, W. D., Bismayer, U., Boatner, L. A., Isaacson, S. G., & Ewing, R. C. (2016). Anisotropic mechanical properties of zircon and the effect of radiation damage. *Physics and Chemistry of Minerals*, 43(9), 627–638. https://doi.org/10.1007/s00269-016-0822-9
- Beyssac, O., Goffé, B., Chopin, C., & Rouzaud, J. N. (2002). Raman spectra of carbonaceous material in metasediments: A new geothermometer. *Journal of Metamorphic Geology*, 20(9), 859–871. https://doi.org/10.1046/j.1525-1314.2002.00408.x
- Bonazzi, M., Tumiati, S., Thomas, J., Angel, R. J., & Alvaro, M. (2019). Assessment of the reliability of elastic geobarometry with quartz inclusions. *Lithos*, 350–351, 105201. https://doi.org/10.1016/j.lithos.2019.105201
- Bröcker, M., & Enders, M. (1999). U-Pb zircon geochronology of unusual eclogite-facies rocks from Syros and Tinos (Cyclades, Greece). Geological Magazine, 136(2), 111–118. https://doi.org/10.1017/S0016756899002320
- Brunet, F., Allan, D. R., Redfern, S. A. T., Angel, R. J., Miletich, R., Reichmann, H. J., et al. (1999). Compressibility and thermal expansivity of synthetic apatites, Ca 5 (PO 4) 3 X with X = OH, F and Cl. European Journal of Mineralogy, 11(6), 1023–1036. https://doi.org/10.1127/ejm/11/6/1023
- Campomenosi, N., Mazzucchelli, M. L., Mihailova, B., Scambelluri, M., Angel, R. J., Nestola, F., et al. (2018). How geometry and anisotropy affect residual strain in host-inclusion systems: Coupling experimental and numerical approaches. *American Mineralogist*, 103(12), 2032–2035. https://doi.org/10.2138/am-2018-6700CCBY
- Carswell, D. A., Tucker, R. D., O'Brien, P. J., & Krogh, T. E. (2003). Coesite micro-inclusions and the U/Pb age of zircons from the Hareidland Eclogite in the Western Gneiss Region of Norway. *Lithos*, 67(3–4), 181–190. https://doi.org/10.1016/S0024-4937(03)00014-8
- Cisneros, M., Ashley, K. T., & Bodnar, R. J. (2020). Evaluation and application of the quartz-inclusions-in-epidote mineral barometer. American Mineralogist, 105(8), 1140–1151. https://doi.org/10.2138/am-2020-7379
- Cohen, L. H., & Rosenfeld, J. L. (1979). Diamond: Depth of crystallization inferred from compressed included garnet. The Journal of Geology, 87(3), 333–340. https://doi.org/10.1086/628422
- Comodi, P., Liu, Y., & Frezzotti, M. L. (2001). Structural and vibrational behaviour of fluorapatite with pressure. Part II: In situ micro-Raman spectroscopic investigation. *Physics and Chemistry of Minerals*, 28(4), 225–231. https://doi.org/10.1007/s002690100155
- Cressey, G., Schmid, R., & Wood, B. J. (1978). Thermodynamic properties of almandine-grossular garnet solid solutions. Contributions to Mineralogy and Petrology, 67(4), 397–404. https://doi.org/10.1007/BF00383299
- Enami, M., Nishiyama, T., & Mouri, T. (2007). Laser Raman microspectrometry of metamorphic quartz: A simple method for comparison of metamorphic pressures. American Mineralogist, 92(8–9), 1303–1315. https://doi.org/10.2138/am.2007.2438
- Ferry, J. M., & Spear, F. S. (1978). Experimental calibration of the partitioning of Fe and Mg between biotite and garnet. *Contributions to Mineralogy and Petrology*, 66(2), 113–117. https://doi.org/10.1007/BF00372150
- Frank, O., Zukalova, M., Laskova, B., Kürti, J., Koltai, J., & Kavan, L. (2012). Raman spectra of titanium dioxide (anatase, rutile) with identified oxygen isotopes (16, 17, 18). Physical Chemistry Chemical Physics, 14(42), 14,567–14,572. https://doi.org/10.1039/C2CP42763J
- Franz, G., & Liebscher, A. (2004). Physical and chemical properties of the epidote minerals—An introduction. *Reviews in Mineralogy and Geochemistry*, 56(1), 1–81. https://doi.org/10.2138/gsrmg.56.1.1
- Freeman, J. J., Wang, A., Kuebler, K. E., Jolliff, B. L., & Haskin, L. A. (2008). Characterization of natural feldspars by Raman spectroscopy for future planetary exploration. *The Canadian Mineralogist*, 46(6), 1477–1500, https://doi.org/10.3749/canmin.46.6.1477
- Gatta, G. D., Merlini, M., Lee, Y., & Poli, S. (2011). Behavior of epidote at high pressure and high temperature: A powder diffraction study up to 10 GPa and 1,200 K. *Physics and Chemistry of Minerals*, 38(6), 419–428. https://doi.org/10.1007/s00269-010-0415-y
- Geiger, C. A. (2000). Volumes of mixing in aluminosilicate garnets: Solid solution and strain behavior. *American Mineralogist*, 85(7–8), 893–897. https://doi.org/10.2138/am-2000-0702
- Gryger, K. J. (2017). Spatial variability of the depth to the magma reservoir beneath the Yellowstone Caldera inferred from observations of seiche loading induced strain. LSU Master's Theses, (4495). Retrieved from https://digitalcommons.lsu.edu/gradschool_theses/4495
- Gualda, G. A. R., Ghiorso, M. S., Lemons, R. V., & Carley, T. L. (2012). Rhyolite-MELTS: A modified calibration of MELTS optimized for silica-rich, fluid-bearing magmatic systems. *Journal of Petrology*, 53(5), 875–890. https://doi.org/10.1093/petrology/egr080
- Guiraud, M., & Powell, R. (2006). P-V-T relationships and mineral equilibria in inclusions in minerals. Earth and Planetary Science Letters, 244(3-4), 683-694. https://doi.org/10.1016/j.epsl.2006.02.021
- Hacker, B. R., Andersen, T. B., Johnston, S., Kylander-Clark, A. R. C., Peterman, E. M., Walsh, E. O., & Young, D. (2010). High-temperature deformation during continental-margin subduction & exhumation: The ultrahigh-pressure Western Gneiss Region of Norway. Tectonophysics, 480(1-4), 149-171. https://doi.org/10.1016/j.tecto.2009.08.012
- Harris, J. W., & Munn, R. W. (1970). Thermal expansion of garnets included in diamond. *Journal of Geophysical Research*, 75(29), 5775–5792. https://doi.org/10.1029/JB075i029p05775
- Hemley, R. J. (2013). Pressure dependence of Raman spectra of SiO₂ polymorphs: α-quartz, coesite, and stishovite. High-Pressure Research in Mineral Physics: A Volume in Honor of Syun-iti Akimoto, 39. https://doi.org/10.1029/GM039p0347
- Holland, T. J. B. (1980). The reaction albite = jadeite + quartz determined experimentally in the range 600–1200°C. *American Mineralogist*, 65(1–2), 129–134.

CISNEROS AND BEFUS 19 of 21



- Holland, T. J. B., & Powell, R. (1996a). Thermodynamics of order-disorder in minerals: I. Symmetric formalism applied to minerals of fixed composition. *American Mineralogist*, 81(11–12), 1413–1424. https://doi.org/10.2138/am-1996-11-1214
- Holland, T. J. B., & Powell, R. (1996b). Thermodynamics of order-disorder in minerals: II. Symmetric formalism applied to solid solutions. American Mineralogist, 81(11–12), 1425–1437. https://doi.org/10.2138/am-1996-11-1215
- Holland, T. J. B., & Powell, R. (1998). An internally consistent thermodynamic data set for phases of petrological interest. *Journal of Metamorphic Geology*, 16(3), 309–343. https://doi.org/10.1111/j.1525-1314.1998.00140.x
- Holland, T. J. B., & Powell, R. (2011). An improved and extended internally consistent thermodynamic dataset for phases of petrological interest, involving a new equation of state for solids. *Journal of Metamorphic Geology*, 29(3), 333–383. https://doi.org/10.1111/j.1525-1314.2010.00923.x
- Hovis, G., Abraham, T., Hudacek, W., Wildermuth, S., Scott, B., Altomare, C., et al. (2015). Thermal expansion of F-Cl apatite crystalline solutions. *American Mineralogist*, 100(5–6), 1040–1046. https://doi.org/10.2138/am-2015-5176
- Hovis, G. L., Scott, B. T., Altomare, C. M., Leaman, A. R., Morris, M. D., Tomaino, G. P., & McCubbin, F. M. (2014). Thermal expansion of fluorapatite-hydroxylapatite crystalline solutions. *American Mineralogist*, 99(11–12), 2171–2175. https://doi.org/10.2138/am-2014-4914
- Howell, D., Wood, I. G., Dobson, D. P., Jones, A. P., Nasdala, L., & Harris, J. W. (2010). Quantifying strain birefringence halos around inclusions in diamond. *Contributions to Mineralogy and Petrology*, 160(5), 705–717. https://doi.org/10.1007/s00410-010-0503-5
- Isaak, D. G., Anderson, O. L., & Oda, H. (1992). High-temperature thermal expansion and elasticity of calcium-rich garnets. *Physics and Chemistry of Minerals*, 19(2), 106–120. https://doi.org/10.1007/BF00198608
- Izraeli, E. S., Harris, J. W., & Navon, O. (1999). Raman barometry of diamond formation. Earth and Planetary Science Letters, 173(3), 351–360. https://doi.org/10.1016/S0012-821X(99)00235-6
- Javoy, M. (1977). Stable isotopes and geothermometry. *Journal of the Geological Society*, 133(6), 609–636. https://doi.org/10.1144/gsjgs.133.6.0609
- Kohn, M. J. (2014). "Thermoba-Raman-try": Calibration of spectroscopic barometers and thermometers for mineral inclusions. Earth and Planetary Science Letters, 388(supplement C), 187–196. https://doi.org/10.1016/j.epsl.2013.11.054
- Krogh, E. J. (1982). Metamorphic evolution of Norwegian country-rock eclogites, as deduced from mineral inclusions and compositional zoning in garnets. Lithos, 15(4), 305–321. https://doi.org/10.1016/0024-4937(82)90021-4
- Kroumova, E., Aroyo, M. I., Perez-Mato, J. M., Kirov, A., Capillas, C., Ivantchev, S., & Wondratschek, H. (2003). Bilbao crystallographic server: Useful databases and tools for phase-transition studies. *Phase Transitions*, 76(1–2), 155–170. https://doi.org/10.1080/0141159031000076110
- Kylander-Clark, A. R. C., Hacker, B. R., & Mattinson, J. M. (2008). Slow exhumation of UHP terranes: Titanite and rutile ages of the Western gneiss region, Norway. Earth and Planetary Science Letters, 272(3-4), 531–540. https://doi.org/10.1016/j.epsl.2008.05.019
- Laurent, V., Lanari, P., Naïr, I., Augier, R., Lahfid, A., & Jolivet, L. (2018). Exhumation of eclogite and blueschist (Cyclades, Greece): Pressure-temperature evolution determined by thermobarometry and garnet equilibrium modelling. *Journal of Metamorphic Geology*, 36(6), 769–798. https://doi.org/10.1111/jmg.12309
- Liu, J., Glasmacher, U. A., Lang, M., Trautmann, C., Voss, K.-O., Neumann, R., et al. (2008). Raman spectroscopy of apatite irradiated with swift heavy ions with and without simultaneous exertion of high pressure. *Applied Physics A*, 91(1), 17–22. https://doi.org/10.1007/s00339-008-4402-9
- Liu, L.-G., & Mernagh, T. P. (1992). Phase transitions and Raman spectra of anatase and rutile at high pressures and room temperature. European Journal of Mineralogy, 4(1), 45–52. https://doi.org/10.1127/ejm/4/1/0045
- Luttrell, K., Mencin, D., Francis, O., & Hurwitz, S. (2013). Constraints on the upper crustal magma reservoir beneath Yellowstone Caldera inferred from lake-seiche induced strain observations. *Geophysical Research Letters*, 40, 501–506. https://doi.org/10.1002/grl.50155
- Mao, Z., Jiang, F., & Duffy, T. S. (2007). Single-crystal elasticity of zoisite Ca2Al3Si3O12 (OH) by Brillouin scattering. American Mineralogist, 92(4), 570–576. https://doi.org/10.2138/am.2007.2329
- Mazzucchelli, M. L., Burnley, P., Angel, R. J., Morganti, S., Domeneghetti, M. C., Nestola, F., & Alvaro, M. (2018). Elastic geothermobarometry: Corrections for the geometry of the host-inclusion system. *Geology*, 46(3), 231–234. https://doi.org/10.1130/G39807.1
- Mazzucchelli, M. L., Reali, A., Morganti, S., Angel, R. J., & Alvaro, M. (2019). Elastic geobarometry for anisotropic inclusions in cubic hosts. Lithos, 350–351, 105218. https://doi.org/10.1016/j.lithos.2019.105218
- McKeown, D. A. (2005). Raman spectroscopy and vibrational analyses of albite: From 25°C through the melting temperature. American Mineralogist, 90(10), 1506–1517. https://doi.org/10.2138/am.2005.1726
- Milani, S., Nestola, F., Alvaro, M., Pasqual, D., Mazzucchelli, M. L., Domeneghetti, M. C., & Geiger, C. A. (2015). Diamond-garnet geo-barometry: The role of garnet compressibility and expansivity. Lithos, 227, 140–147. https://doi.org/10.1016/j.lithos.2015.03.017
- Milani, S., Angel, R. J., Scandolo, L., Mazzucchelli, M. L., Ballaran, T. B., Klemme, S., et al. (2017). Thermo-elastic behavior of grossular garnet at high pressures and temperatures. *American Mineralogist*, 102(4), 851–859. https://doi.org/10.2138/am-2017-5855
- Murri, M., Mazzucchelli, M. L., Campomenosi, N., Korsakov, A. V., Prencipe, M., Mihailova, B. D., et al. (2018). Raman elastic geobarometry for anisotropic mineral inclusions. *American Mineralogist*, 103(11), 1869–1872. https://doi.org/10.2138/am-2018-6625CCBY
- Myers, M. L., Wallace, P. J., Wilson, C. J. N., Morter, B. K., & Swallow, E. J. (2016). Prolonged ascent and episodic venting of discrete magma batches at the onset of the Huckleberry Ridge supereruption, Yellowstone. *Earth and Planetary Science Letters*, 451, 285–297. https://doi.org/10.1016/j.epsl.2016.07.023
- Nestola, F., Prencipe, M., Nimis, P., Sgreva, N., Perritt, S. H., Chinn, I. L., & Zaffiro, G. (2018). Toward a robust elastic geobarometry of kyanite inclusions in eclogitic diamonds. *Journal of Geophysical Research: Solid Earth*, 123, 6411–6423. https://doi.org/10.1029/ 2018JB016012
- Nestola, F., Nimis, P., Ziberna, L., Longo, M., Marzoli, A., Harris, J. W., et al. (2011). First crystal-structure determination of olivine in diamond: Composition and implications for provenance in the Earth's mantle. *Earth and Planetary Science Letters*, 305(1–2), 249–255. https://doi.org/10.1016/j.epsl.2011.03.007
- Nestola, F., Zaffiro, G., Mazzucchelli, M. L., Nimis, P., Andreozzi, G. B., Periotto, B., et al. (2019). Diamond-inclusion system recording old deep lithosphere conditions at Udachnaya (Siberia). Scientific Reports, 9(1), 12,586–12,588. https://doi.org/10.1038/s41598-019-48778-x
- Pawley, A. R., Redfern, S. A. T., & Holland, T. J. B. (1996). Volume behavior of hydrous minerals at high pressure and temperature: I. Thermal expansion of lawsonite, zoisite, clinozoisite, and diaspore. *American Mineralogist*, 81(3–4), 335–340. https://doi.org/10.2138/am-1996-3-407
- Putlitz, B., Cosca, M. A., & Schumacher, J. C. (2005). Prograde mica 40Ar/39Ar growth ages recorded in high pressure rocks (Syros, Cyclades, Greece). Chemical Geology, 214(1–2), 79–98. https://doi.org/10.1016/j.chemgeo.2004.08.056
- Qin, F., Wu, X., Wang, Y., Fan, D., Qin, S., Yang, K., et al. (2016). High-pressure behavior of natural single-crystal epidote and clinozoisite up to 40 GPa. *Physics and Chemistry of Minerals*, 43(9), 649–659. https://doi.org/10.1007/s00269-016-0824-7

CISNEROS AND BEFUS 20 of 21



- Rosenfeld, J. L. (1969). Stress effects around quartz inclusions in almandine and the piezothermometry of coexisting aluminum silicates. American Journal of Science, 267(3), 317–351. https://doi.org/10.2475/ajs.267.3.317
- Rosenfeld, J. L., & Chase, A. B. (1961). Pressure and temperature of crystallization from elastic effects around solid inclusions in minerals? American Journal of Science, 259(7), 519–541. https://doi.org/10.2475/ajs.259.7.519
- Runyon, S. E., Nickerson, P. A., Seedorff, E., Barton, M. D., Mazdab, F. K., Lecumberri-Sánchez, P., & Steele-MacInnis, M. (2019). Sodic-calcic family of alteration in porphyry systems of Arizona and adjacent New Mexico. *Economic Geology*, 114(4), 745–770. https://doi.org/10.5382/econgeo.4661
- Ryzhova, T. V., Aleksandrov, K. S., & Korobkova, V. M. (1966). The elastic properties of rock-forming minerals; V, additional data on silicates. *Physics of the Solid Earth*, 2, 63–65.
- Samara, G. A., & Peercy, P. S. (1973). Pressure and temperature dependence of the static dielectric constants and Raman spectra of TiO₂ (rutile). *Physical Review B*, 7(3), 1131–1148. https://doi.org/10.1103/PhysRevB.7.1131
- Schmidt, C., & Ziemann, M. A. (2000). In-situ Raman spectroscopy of quartz: A pressure sensor for hydrothermal diamond-anvil cell experiments at elevated temperatures. *American Mineralogist*, 85(11–12), 1725–1734. https://doi.org/10.2138/am-2000-11-1216
- Schouwink, P., Miletich, R., Ullrich, A., Glasmacher, U. A., Trautmann, C., Neumann, R., & Kohn, B. P. (2010). Ion tracks in apatite at high pressures: The effect of crystallographic track orientation on the elastic properties of fluorapatite under hydrostatic compression. *Physics and Chemistry of Minerals*, 37(6), 371–387. https://doi.org/10.1007/s00269-009-0340-0
- Schumacher, J. C., Brady, J. B., Cheney, J. T., & Tonnsen, R. R. (2008). Glaucophane-bearing marbles on Syros, Greece. *Journal of Petrology*, 49(9), 1667–1686. https://doi.org/10.1093/petrology/egn042
- Shamloo, H. I., & Till, C. B. (2019). Decadal transition from quiescence to supereruption: Petrologic investigation of the Lava Creek Tuff, Yellowstone Caldera, WY. Contributions to Mineralogy and Petrology, 174(4), 32. https://doi.org/10.1007/s00410-019-1570-x
- Soukis, K., & Stockli, D. F. (2013). Structural and thermochronometric evidence for multi-stage exhumation of southern Syros, Cycladic islands, Greece. Tectonophysics, 595–596, 148–164. https://doi.org/10.1016/j.tecto.2012.05.017
- Speziale, S., Duffy, T. S., & Angel, R. J. (2004). Single-crystal elasticity of fayalite to 12 GPa. *Journal of Geophysical Research*, 109, B12202. https://doi.org/10.1029/2004JB003162
- Stangarone, C., Angel, R. J., Prencipe, M., Campomenosi, N., Mihailova, B., & Alvaro, M. (2019). Measurement of strains in zircon inclusions by Raman spectroscopy. European Journal of Mineralogy, 31(4), 685–694. https://doi.org/10.1127/ejm/2019/0031-2851
- Swamy, V., Kuznetsov, A., Dubrovinsky, L. S., Caruso, R. A., Shchukin, D. G., & Muddle, B. C. (2005). Finite-size and pressure effects on the Raman spectrum of nanocrystalline anatase TiO₂. *Physical Review B*, 71(18), 184,302. https://doi.org/10.1103/PhysRevB.71.184302
- Thomas, J. B., & Spear, F. S. (2018). Experimental study of quartz inclusions in garnet at pressures up to 3.0 GPa: Evaluating validity of the quartz-in-garnet inclusion elastic thermobarometer. *Contributions to Mineralogy and Petrology*, 173(5), 42. https://doi.org/10.1007/s00410-018-1469-v
- Tsujimori, T., Sisson, V. B., Liou, J. G., Harlow, G. E., & Sorensen, S. S. (2006). Very-low-temperature record of the subduction process: A review of worldwide lawsonite eclogites. *Lithos*, 92(3–4), 609–624. https://doi.org/10.1016/j.lithos.2006.03.054
- Van der Molen, I., & Van Roermund, H. L. M. (1986). The pressure path of solid inclusions in minerals: The retention of coesite inclusions during uplift. *Lithos*, 19(3–4), 317–324. https://doi.org/10.1016/0024-4937(86)90030-7
- Vazquez, J. A., Kyriazis, S. F., Reid, M. R., Sehler, R. C., & Ramos, F. C. (2009). Thermochemical evolution of young rhyolites at Yellowstone: Evidence for a cooling but periodically replenished postcaldera magma reservoir. *Journal of Volcanology and Geothermal Research*, 188(1–3), 186–196. https://doi.org/10.1016/j.jvolgeores.2008.11.030
- Wain, A., Waters, D., Jephcoat, A., & Olijynk, H. (2000). The high-pressure to ultrahigh-pressure eclogite transition in the Western Gneiss Region, Norway. European Journal of Mineralogy, 12(3), 667–687. https://doi.org/10.1127/0935-1221/2000/0012-0667
- Wang, Z., & Ji, S. (2001). Elasticity of six polycrystalline silicate garnets at pressure up to 3.0 GPa. American Mineralogist, 86(10), 1209–1218. https://doi.org/10.2138/am-2001-1009
- Wolfe, O. M., & Spear, F. S. (2018). Determining the amount of overstepping required to nucleate garnet during Barrovian regional metamorphism, Connecticut Valley Synclinorium. *Journal of Metamorphic Geology*, 36(1), 79–94. https://doi.org/10.1111/jmg.12284
- Zaffiro, G., Angel, R. J., & Alvaro, M. (2019). Constraints on the equations of state of stiff anisotropic minerals: Rutile, and the implications for rutile elastic barometry. *Mineralogical Magazine*, 83(03), 339–347. https://doi.org/10.1180/mgm.2019.24
- Zha, C.-S., Duffy, T. S., Downs, R. T., Mao, H.-K., & Hemley, R. J. (1996). Sound velocity and elasticity of single-crystal forsterite to 16 GPa. Journal of Geophysical Research: Solid Earth, 101(B8), 17,535–17,545. https://doi.org/10.1029/96JB01266
- Zhang, Y. (1998). Mechanical and phase equilibria in inclusion-host systems. Earth and Planetary Science Letters, 157(3–4), 209–222. https://doi.org/10.1016/S0012-821X(98)00036-3
- Zhong, X., Andersen, N. H., Dabrowski, M., & Jamtveit, B. (2019). Zircon and quartz inclusions in garnet used for complementary Raman thermobarometry: Application to the Holsnøy eclogite, Bergen arcs, Western Norway. *Contributions to Mineralogy and Petrology*, 174(6), 50. https://doi.org/10.1007/s00410-019-1584-4
- Zhong, X., Moulas, E., & Tajčmanová, L. (2018). Tiny timekeepers witnessing high-rate exhumation processes. *Scientific Reports*, 8(1), 2234. https://doi.org/10.1038/s41598-018-20291-7
- Zhong, X., Moulas, E., & Tajčmanová, L. (2020). Post-entrapment modification of residual inclusion pressure and its implications for Raman elastic thermobarometry. *Solid Earth*, 11(1), 223–240. https://doi.org/10.5194/se-11-223-2020
- Zhukov, V. P., & Korsakov, A. V. (2015). Evolution of host-inclusion systems: A visco-elastic model. *Journal of Metamorphic Geology*, 33(8), 815–828. https://doi.org/10.1111/jmg.12149

CISNEROS AND BEFUS 21 of 21